

Quasiparticles in superconducting qubits with asymmetric junctions

Giampiero Marchegiani*

Quantum Research Centre, Technology Innovation Institute, Abu Dhabi, UAE

Luigi Amico

Quantum Research Centre, Technology Innovation Institute, Abu Dhabi, UAE

Centre for Quantum Technologies, National University of Singapore, 3 Science Drive 2, Singapore 117543

INFN-Sezione di Catania, Via S. Sofia 64, 95127 Catania, Italy

*LANEF ‘Chaire d’excellence’, Université Grenoble-Alpes & CNRS, F-38000 Grenoble, France and
MajuLab, CNRS-UNS-NUS-NTU International Joint Research Unit, UMI 3654, Singapore*

Gianluigi Catelani

JARA Institute for Quantum Information (PGI-11),

Forschungszentrum Jülich, 52425 Jülich, Germany and

Quantum Research Centre, Technology Innovation Institute, Abu Dhabi, UAE

(Dated: May 13, 2022)

Designing the spatial profile of the superconducting gap – gap engineering – has long been recognized as an effective way of controlling quasiparticles in superconducting devices. In aluminum films, their thickness modulates the gap; therefore, standard fabrication of Al/AlOx/Al Josephson junctions, which relies on overlapping a thicker film on top of a thinner one, always results in gap-engineered devices. Here we reconsider quasiparticle effects in superconducting qubits to explicitly account for the unavoidable asymmetry in the gap on the two sides of a Josephson junction. We find that different regimes can be encountered in which the quasiparticles have either similar densities in the two junction leads, or are largely confined to the lower-gap lead. Qualitatively, for similar densities the qubit’s excited state population is lower but its relaxation rate higher than when the quasiparticles are confined; therefore, there is a potential trade-off between two desirable properties in a qubit.

I. INTRODUCTION

Various superconducting materials have been investigated over the last several years to manufacture components of superconducting circuits: resonators can be made out of TiN [1], NbTiN [2, 3], and granular Al [4–6], capacitor pads out of TiN [7], Nb [8, 9], and Ta [10–12], and inductances out of NbN [13, 14], NbTiN [15, 16], and granular Al [17]. However, the central elements of qubits, the Josephson junctions, are generally based on aluminum/aluminum oxide/aluminum structures, as the native oxide of aluminum results in high-quality and reproducible tunnel barriers. Moreover, Al displays an almost ideal behaviour in comparison to the original Bardeen-Cooper-Schrieffer (BCS) model [18], and effects due to, for instance, Fermi-liquid renormalization of the spin susceptibility and spin-orbit scattering can be incorporated in the modeling of the superconducting properties (see *e.g.* [19] and references therein). In the typical fabrication process, a junction is realized by first depositing a layer of thickness d_L on the substrate; after oxidation, a second layer is evaporated on top of the structure (see inset of Fig. 1), with thickness $d_R > d_L$ to ensure that the top layer is electrically continuous. For thin Al films, it is well known that the superconducting critical temperature T_c , and hence the energy gap

$\Delta = 1.764k_B T_c$, depend on the film thickness [20]. For thickness greater than ~ 3 nm, the phenomenological dependence of the Al gap on thickness d is of the form $\Delta(d) = \Delta_{\text{bulk}} + ad^{-1}$, where $\Delta_{\text{bulk}} \simeq 180 \mu\text{eV}$ is the gap in the bulk limit, and a is a parameter whose value depends on the details of the deposition process [20–24]. In Fig. 1, we display measurements of thin-film Al gap reported in the literature [21, 24] (points), and compare them to the value calculated using the previous expression with $a \simeq 600 \mu\text{eV}\cdot\text{nm}$ (solid line). In actual devices, the frequency associated with the gap asymmetry $\omega_{LR}/(2\pi) = (\Delta_L - \Delta_R)/h$ can be of the order of a few GHz (here h is the Planck’s constant). For instance, in a Josephson junction with $d_L = 20$ nm and $d_R = 60$ nm, our phenomenological expression gives approximately $\omega_{LR} \approx 2\pi \cdot 5$ GHz, which is comparable to typical qubit frequencies, and hence potentially harmful to the qubit operation, as we will show. In this work, we extensively discuss the effect of gap asymmetry onto the qubit properties, focusing on all-Al devices.

The gap asymmetry introduces the new energy scale ω_{LR} in the description of the system, in addition to the qubit frequency ω_{10} and the (effective) temperature T (hereinafter we set $\hbar = k_B = 1$, where \hbar , k_B are the reduced Planck’s constant and the Boltzmann constant, respectively). If ω_{LR} is the smallest scale, the gap asymmetry can be neglected. Since the condition $\omega_{10} > T$ is typically fulfilled for the proper qubit operation, there are only two possibilities to address: I. $\omega_{LR} > \omega_{10} > T$

* giampiero.marchegiani@tii.ae

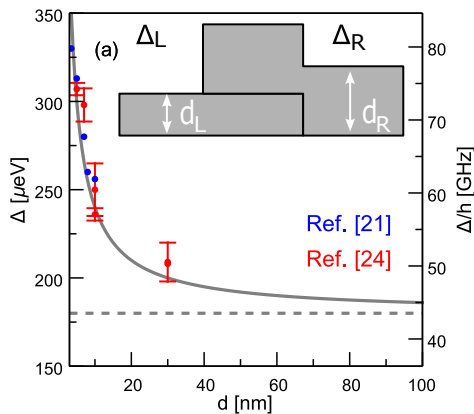


FIG. 1. Superconducting gap (Δ) vs thickness (d) in a typical Al thin film. For $d \lesssim 100$ nm, as the thickness decreases the gap increases as $1/d$ above the bulk value $\Delta_{\text{bulk}} \simeq 180 \mu\text{eV}$. Inset: schematic representation of an Al junction deposited through electron beam evaporation. To ensure a good overlap in the junction region, the thickness of the second layer (d_R) is larger than the first evaporated layer (d_L), hence resulting in a gap difference between the two leads of the junction ($\Delta_L > \Delta_R$).

or II. $\omega_{10} > \omega_{LR} > T$. Clearly case I is the farthest one from the equal gap (or symmetric) situation: as we will show below, the quasiparticles are largely trapped in the lead with the lowest gap. Indeed, the qubit transition cannot give sufficient energy to the quasiparticles to escape to the other lead, due to the large gap asymmetry. On the one hand, the trapped quasiparticles cannot contribute to the qubit relaxation rate, so the qubit lifetime can be longer. On the other hand, the exclusion of a possible relaxation mechanism is associated with an increased, and possibly high, residual excited state population of the qubit. The case II will turn out to be more complex: the quasiparticles can have similar densities in both leads, or again be trapped, depending on the interplay between generation at the junction (via the absorption of pair-breaking photons), recombination, and relaxation. Qualitatively, for slow generation the quasiparticles can again be trapped, while for sufficiently fast generation and/or sufficiently small gap asymmetry the quasiparticles populate both leads with similar densities. Despite this complexity, the condition $\omega_{10} > \omega_{LR}$ ensures the qubit relaxation can be mediated by quasiparticle tunneling, leading to higher qubit decay rate and lower excited state population than for $\omega_{10} < \omega_{LR}$ (if other parameters are not changed). Our main goal is the quantitative analysis of the two cases, using realistic parameters; in particular, we re-examine a previously published experiment in light of our results for case II, before extending our study to encompass case I.

The article is organized as follows. In Sec. II we review the microscopic model for the qubit-quasiparticle interaction, generalizing the main results to the case of leads with asymmetric gaps. The model for the dynamics

of the quasiparticle density is developed in Sec. III, accounting for the gap difference in the leads. The steady state for the qubit-quasiparticle system is then analyzed in Sec. IV. The case of a split transmon, whose frequency can be controlled on chip, is discussed in Sec. V. We finally summarize our results in Sec. VI.

II. MICROSCOPIC MODEL

In this section we briefly review the microscopic model describing the interaction between the low-energy modes of a superconducting qubit and quasiparticle excitations to establish our notation and to generalize the approach to the case of unequal gaps on the two sides of a junction. We consider for concreteness a single-junction transmon qubit [25]; however, the approach can be extended to arbitrary qubit design, see Refs. [26, 27], and Sec. V for the two-junction split transmon. In the single-junction case, the low-energy Hamiltonian is

$$\hat{H} = \hat{H}_\varphi + \hat{H}_{\text{qp}} + \hat{H}_T. \quad (1)$$

In the absence of quasiparticles, $\hat{H}_\varphi = 4E_C(\hat{N} - n_g)^2 - E_J \cos \hat{\varphi}$ describes the qubit dynamics, where E_C, E_J are the charging and the Josephson energy, respectively. Here, $\hat{N} = -id/d\varphi$ is the number operator of Cooper pairs tunneling across the junction, and n_g is the dimensionless gate voltage.

The quasiparticle term \hat{H}_{qp} is the sum of the mean-field BCS quasiparticle Hamiltonians for the left and right electrodes,

$$\hat{H}_{\text{qp}} = \sum_{\alpha=L,R} \hat{H}_{\text{qp}}^\alpha, \quad \hat{H}_{\text{qp}}^\alpha = \sum_{n,\sigma} \epsilon_n^\alpha \hat{\gamma}_{n\sigma}^\alpha \hat{\gamma}_{n\sigma}^{\alpha\dagger}. \quad (2)$$

Here $\hat{\gamma}_{n\sigma}^\alpha$ ($\hat{\gamma}_{n\sigma}^{\alpha\dagger}$) is the quasiparticle annihilation (creation) operator, $\sigma = \uparrow, \downarrow$ accounts for spin, and the quasiparticle energies are $\epsilon_n^\alpha = \sqrt{(\xi_n^\alpha)^2 + \Delta_\alpha^2}$, with ξ_n^α and Δ_α being the single-particle energy level n in the normal state of electrode α , and the gap parameter in that electrode, respectively. Finally, the tunneling term \hat{H}_T describes single quasiparticle tunneling across the junction,

$$\hat{H}_T = t \sum_{n,m,\sigma} \left(e^{i\frac{\hat{\varphi}}{2}} u_n^L u_m^R - e^{-i\frac{\hat{\varphi}}{2}} v_m^R v_n^L \right) \hat{\gamma}_{n\sigma}^{L\dagger} \hat{\gamma}_{m\sigma}^R + \text{H.c.}, \quad (3)$$

while pair tunneling has already been taken into account by including the Josephson energy term in \hat{H}_φ (see Appendix A in Ref. [27] for more details). The tunneling amplitude t is related to the normal-state junction conductance by $g_T = 4\pi e^2 \nu^L \nu^R \mathcal{V}_L \mathcal{V}_R t^2$ [28], with e the electron's charge and \mathcal{V}_L (\mathcal{V}_R) volume of the left(right) lead. We assume identical densities of states per spin direction and unit volume in the leads, $\nu^L = \nu^R = \nu_0$. The tunneling term, Eq. (3), couples the qubit to the quasiparticles; therefore, a transition between initial, $|i\rangle$, and final, $|f\rangle$, qubit states of energies ω_i and ω_f becomes possible when

a quasiparticle tunnels through the junction. We will restrict our considerations to the lowest energy states of the transmon system. These states can be classified in terms of their logical value being 0 or 1 (with the 1 state having higher energy), and their parity being even (e) or odd (o) [29], as schematically depicted in Fig. 2d. Here parity refers to the number of electrons having crossed the junction, so every single quasiparticle tunneling event changes the parity of the transmon. We recall that in transmons the energy difference between states of different parity but same logical value is exponentially suppressed with $E_J/E_C \gg 1$ and will be neglected [29].

The transition rate Γ_{if} can be calculated using Fermi's Golden Rule, yielding [29, 30]

$$\Gamma_{if} = \left| \langle f | \sin \frac{\hat{\varphi}}{2} | i \rangle \right|^2 S_{\text{qp}}^+(\omega_{if}) + \left| \langle f | \cos \frac{\hat{\varphi}}{2} | i \rangle \right|^2 S_{\text{qp}}^-(\omega_{if}), \quad (4)$$

where $\omega_{if} = \omega_i - \omega_f$. The normalized spectral current density S_{qp}^\pm is the sum of the contributions from the two electrodes $S_{\text{qp}}^\pm(\omega) = \sum_{\alpha=L,R} S_\alpha^\pm(\omega)$, where

$$S_\alpha^\pm(\omega) = \frac{2g_T}{e^2} \int_{\Delta_\alpha(\omega)}^{+\infty} d\epsilon \kappa_\alpha^\pm(\epsilon, \epsilon + \omega) f_\alpha(\epsilon) [1 - f_{\bar{\alpha}}(\epsilon + \omega)]. \quad (5)$$

and α identifies the initial location of the quasiparticle involved in the transition. The occupation of the quasiparticle states is determined by the distribution functions $f_\alpha(\xi_n^\alpha) = \langle\langle \hat{\gamma}_{n\uparrow}^{\alpha\dagger} \hat{\gamma}_{n\uparrow}^\alpha \rangle\rangle_{\text{qp}} = \langle\langle \hat{\gamma}_{n\downarrow}^{\alpha\dagger} \hat{\gamma}_{n\downarrow}^\alpha \rangle\rangle_{\text{qp}}$ ($\alpha = L, R$) assumed to be independent of spin, with double angular brackets denoting the averaging over quasiparticle states. In our notation, $\bar{\alpha} = R$ for $\alpha = L$ (and *vice versa*), $\Delta_\alpha(\omega) = \max(\Delta_\alpha, \Delta_{\bar{\alpha}} - \omega)$, and we introduced the function

$$\kappa_\alpha^\pm(\epsilon, \epsilon') = \frac{\epsilon\epsilon' \pm \Delta_\alpha \Delta_{\bar{\alpha}}}{\sqrt{\epsilon^2 - \Delta_\alpha^2} \sqrt{\epsilon'^2 - \Delta_{\bar{\alpha}}^2}}. \quad (6)$$

which accounts for the coherence factors multiplied by the normalized superconducting density of states. The expression in Eq. (4) can be used for qubit relaxation processes ($\omega = \omega_{10} > 0$, with ω_{10} the qubit frequency, downward diagonal arrow in Fig. 2d), excitation ($\omega = -\omega_{10} < 0$, upward diagonal arrow in Fig. 2d) or charge-parity jumps ($|\omega| \ll \omega_{10}$, also known as parity switching events, horizontal arrow in Fig. 2d). The matrix elements were derived in previous works [27, 29] and are reported for convenience in Appendix A.

We consider a typical transmon qubit where the superconducting gaps in the leads of the Josephson junction are different, $\Delta_L \neq \Delta_R$, and discuss the impact of the gap asymmetry on the qubit's transition rates due to quasiparticles. Figure 2a characterizes the relevant frequency scales in our system as a function of the gap ratio $\delta = \Delta_R/\Delta_L$. The transmon frequency $\omega_{10} = \sqrt{8E_J E_C} - E_C$ depends relatively weakly on δ

near $\delta = 1$ through the Josephson energy [31]

$$E_J = \frac{4E_J^0}{\pi} \frac{\delta}{1+\delta} K\left(\frac{|1-\delta|}{1+\delta}\right). \quad (7)$$

Here, $E_J^0 = E_J(\delta = 1) = g_T \Delta_L / (8g_K)$ where $g_K = e^2/(2\pi)$ is the conductance quantum, and $K(x)$ is the complete elliptic integral of the first kind. In contrast, the gap mismatch frequency $\omega_{\text{LR}} = |\Delta_L - \Delta_R|$ increases linearly from zero with the deviation of δ from unity, and can eventually reach the qubit frequency ω_{10} .

We now turn to the transition rates considering separately tunneling from the left (right) to the right (left) electrode. We assume the quasiparticle system in each electrode to be at thermal equilibrium, $f_L(\epsilon) = f_R(\epsilon) = (e^{\epsilon/T} + 1)^{-1}$, with temperature $T = 20$ mK. For visualization purposes, the rates are normalized to the quasiparticle density $x_\alpha \simeq \sqrt{2\pi T}/\Delta_\alpha e^{-\Delta_\alpha/T}$, *i.e.*, $\tilde{\Gamma}_\alpha = \Gamma_\alpha/x_\alpha$ with $\alpha = L, R$; the quasiparticle densities are themselves normalized to the Cooper pair densities in each electrode $n_{\text{Cp}\alpha} = 2\nu_0 \Delta_\alpha$. Consider first the left rates, Fig. 2b: at fixed Δ_L the parity switching rate $\tilde{\Gamma}_{00}^L$ (blue) decreases monotonically with increasing Δ_R , and is exponentially suppressed for $\Delta_R > \Delta_L$, due to the decrease in available states in the right electrode. In contrast, both the qubit relaxation rate $\tilde{\Gamma}_{10}^L$ (green) and the excitation rate $\tilde{\Gamma}_{01}^L$ (yellow) display a non-monotonic evolution with δ . In particular, $\tilde{\Gamma}_{01}^L$ ($\tilde{\Gamma}_{10}^L$) increases monotonically for $\Delta_R < \Delta_L - \omega_{10}$ ($\Delta_R < \Delta_L + \omega_{10}$), and diverges logarithmically due to the gap difference matching the qubit frequency [the matching condition makes the square root singularities in Eq. (6) overlap]; both rates are exponentially suppressed at higher δ . Thus, for gap difference $\Delta_L - \Delta_R \sim \pm \omega_{10}$, the transition rates can be significantly larger than for equal gaps, resulting in a reduced lifetime of the qubit. By symmetry, similar considerations apply to the transition rates from the right electrode upon replacing $L \leftrightarrow R$, see Fig. 2c.

From now on, we set $\Delta_L > \Delta_R$ with no loss of generality. We introduce the quantity T_{qp} to denote the characteristic width of the quasiparticle distribution functions [30, 32]; this effective temperature does not necessarily coincide with the temperature at which samples are cooled in a refrigerator, and we assume it to be the smallest energy scale in the system, $T_{\text{qp}} \ll \Delta_L - \Delta_R, \omega_{10}$. Motivated by the previous analysis, we focus on two different regimes, schematically pictured in Fig. 2e-f using quasiparticle band diagrams. In case I (see Fig. 2e) we have $\Delta_L - \Delta_R - \omega_{10} \gg T_{\text{qp}}$, and all the tunneling processes from the right electrode can be safely neglected. In case II (see Fig. 2f), $\omega_{10} - \Delta_L + \Delta_R \gg T_{\text{qp}}$, the rate $\tilde{\Gamma}_{01}^L$ is suppressed, while qubit relaxation due to quasiparticles tunneling from the right electrode becomes relevant. In the next section we expand this picture, based on (effective) thermal equilibrium, to allow for a more general non-equilibrium situation pertinent to realistic setups.

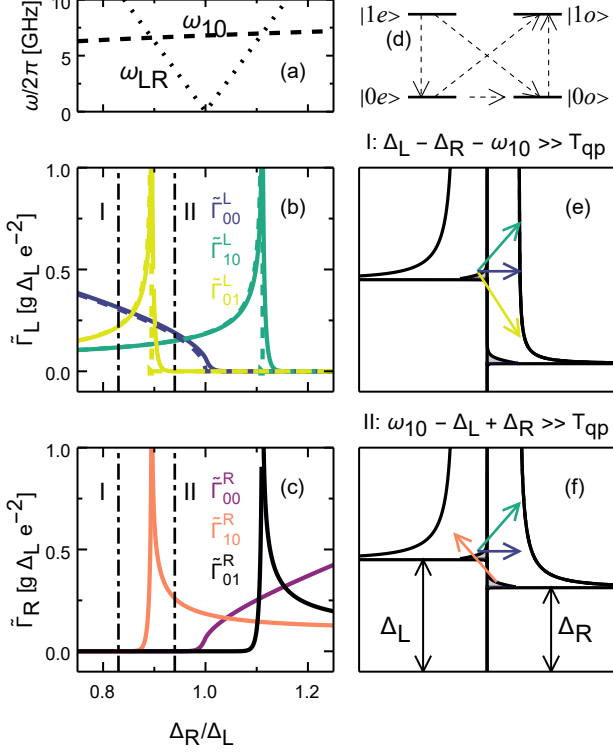


FIG. 2. Gap asymmetry and qubit transition rates in thermal equilibrium. (a) Qubit frequency and gap-difference frequency as a function of the right electrode gap. Qubit transition rates [obtained from Eq. (4) using the matrix elements in Appendix A] associated with quasiparticle tunneling (b) from the left and (c) from the right electrodes as a function of the right electrode gap. The rates can diverge at $\Delta_L - \Delta_R = \pm\omega_{10}$, see text. The analytical expressions for the rates [dashed curves in panel (b)] are given in Appendix B 2. Parameters: $\Delta_L = 260 \mu\text{eV}$, $E_C/h = 300 \text{ MHz}$, $E_J^0 = 70 E_C$, $T = 20 \text{ mK}$. (d) Schematics of the lowest energy states of the qubit with logical state $i = \{0, 1\}$, parity $j = \{e, o\}$, and the corresponding qubit transitions (arrows). Panels (e) and (f) depict the relevant tunneling events for two choices of gap ratio exemplifying cases I and II, respectively [cf. dotted-dashed vertical lines in panels (b) and (c)].

III. QUASIPARTICLE-QUBIT DYNAMICS

The effective equilibrium state of quasiparticles considered in the previous section already makes possible to distinguish two scenarios depending on the relation between qubit frequency and gap difference. In both scenarios, the quasi-elastic transitions from left to right (blue horizontal arrows in Fig. 2e and f) can lead to accumulation of quasiparticles in the right electrode at energies $\gtrsim \Delta_L$, if their relaxation to energies $\sim \Delta_R$ is slow. Moreover, which transitions can take place depends on the qubit state, compare *e.g.* the yellow and green arrows in Fig. 2e. Here we present a general set of equations that governs the coupled dynamics of the qubit and quasiparticles.

Their microscopic origin is discussed in Appendix B.

We begin by considering the evolution equation for the qubit state occupation probability $p_i^j(t)$, with logical state $i = \{0, 1\}$ and parity $j = \{e, o\}$. The rate equation for the probability reads [29, 33]

$$\dot{p}_i^j = -(\Gamma_{\bar{i}\bar{i}}^{j\bar{j}} + \Gamma_{\bar{i}\bar{i}}^{j\bar{j}} + \Gamma_{\bar{i}\bar{i}}^{j\bar{j}})p_i^j + \Gamma_{\bar{i}\bar{i}}^{j\bar{j}}p_{\bar{i}}^{\bar{j}} + \Gamma_{\bar{i}\bar{i}}^{j\bar{j}}p_{\bar{i}}^{\bar{j}} + \Gamma_{\bar{i}\bar{i}}^{j\bar{j}}p_{\bar{i}}^{\bar{j}} \quad (8)$$

where the dot denotes derivative with respect to time, $\bar{i} = i + 1 \pmod{2}$, and $\bar{e} = o$, $\bar{o} = e$. In the transmon regime, the energy difference between even and odd states is small compared to temperature [29], and the transition rates are approximately symmetric under even-odd exchange; that is, we take $\Gamma_{\bar{i}\bar{i}}^{j\bar{j}} = \Gamma_{\bar{i}\bar{i}}^{j\bar{j}}$ and $\Gamma_{\bar{i}\bar{i}}^{j\bar{j}} = \Gamma_{\bar{i}\bar{i}}^{j\bar{j}}$. Summing over the two possible parities, we get the rate equations for the logical state occupation probability $p_i = \sum_{j=\{e,o\}} p_i^j$,

$$\dot{p}_i = -(\Gamma_{\bar{i}\bar{i}}^{eo} + \Gamma_{\bar{i}\bar{i}}^{ee})p_i + (\Gamma_{\bar{i}\bar{i}}^{eo} + \Gamma_{\bar{i}\bar{i}}^{ee})p_{\bar{i}}. \quad (9)$$

The rates in Eq. (9) can be grouped in two categories. The parity conserving terms Γ_{10}^{ee} and Γ_{01}^{ee} (cf. vertical arrows in Fig. 2d) are not associated with quasiparticles, rather, they are linked to a “cold” dissipative environment, $\Gamma_{01}^{ee} \ll \Gamma_{10}^{ee}$ [33]. Conversely, parity-switching events always involve quasiparticles, and the rates have the general expression

$$\Gamma_{\bar{i}\bar{i}'}^{eo} = \Gamma_{\bar{i}\bar{i}'}^{ph} + \tilde{\Gamma}_{\bar{i}\bar{i}'}^L x_L + \tilde{\Gamma}_{\bar{i}\bar{i}'}^{R<} x_{R<} + \tilde{\Gamma}_{\bar{i}\bar{i}'}^{R>} x_{R>}. \quad (10)$$

Here $\Gamma_{\bar{i}\bar{i}'}^{ph}$ accounts for pair-breaking at the junction due to photon-assisted tunneling [34], while the second term in the right-hand side, proportional to the quasiparticle density x_L in the left electrode, accounts for transitions in which a quasiparticle tunnels from the left to the right electrode. The last two terms in Eq. (10) originate from quasiparticles tunneling in the opposite direction (right to left), and we have separated the density in two parts: $x_{R<}$ includes excitations with energy between Δ_R and Δ_L , while $x_{R>}$ those with energy above Δ_L , see Appendix B 1. Explicit formulas for the rates $\tilde{\Gamma}_{\bar{i}\bar{i}'}^\alpha$ are presented in Appendix B 2 (with a slight abuse of notation, α can denote either L and R , or $L, R >$ and $R <$, depending on the quantity to which it is attached).

The time evolution equations for the quasiparticle densities are a generalization of those introduced by Rothwarf and Taylor [35] to phenomenologically account for the interplay between generation and recombination in determining the density of quasiparticles out of equilibrium,

$$\dot{x}_L = g^L - r^L x_L^2 - \delta[(\tilde{\Gamma}_{00}^L + \tilde{\Gamma}_{01}^L)p_0 + (\tilde{\Gamma}_{11}^L + \tilde{\Gamma}_{10}^L)p_1]x_L + \delta[\tilde{\Gamma}_{10}^{R<} p_1 x_{R<} + \delta[\tilde{\Gamma}_{00}^{R>} p_0 + (\tilde{\Gamma}_{11}^{R>} + \tilde{\Gamma}_{10}^{R>})p_1]x_{R>} \quad (11)$$

$$\dot{x}_{R>} = g^{R>} - r^{R>} x_{R>}^2 + [\tilde{\Gamma}_{00}^L p_0 + (\tilde{\Gamma}_{11}^L + \tilde{\Gamma}_{10}^L)p_1]x_L - [\tilde{\Gamma}_{00}^{R>} p_0 + (\tilde{\Gamma}_{11}^{R>} + \tilde{\Gamma}_{10}^{R>})p_1 + \tau_R^{-1}]x_{R>} - r^{<>} x_{R<} x_{R>} \quad (12)$$

$$\dot{x}_{R<} = g^{R<} - r^{R<} x_{R<}^2 + \tau_R^{-1} x_{R>} + \tilde{\Gamma}_{01}^L p_0 x_L - \tilde{\Gamma}_{10}^{R<} p_1 x_{R<} - r^{<>} x_{R<} x_{R>} \quad (13)$$

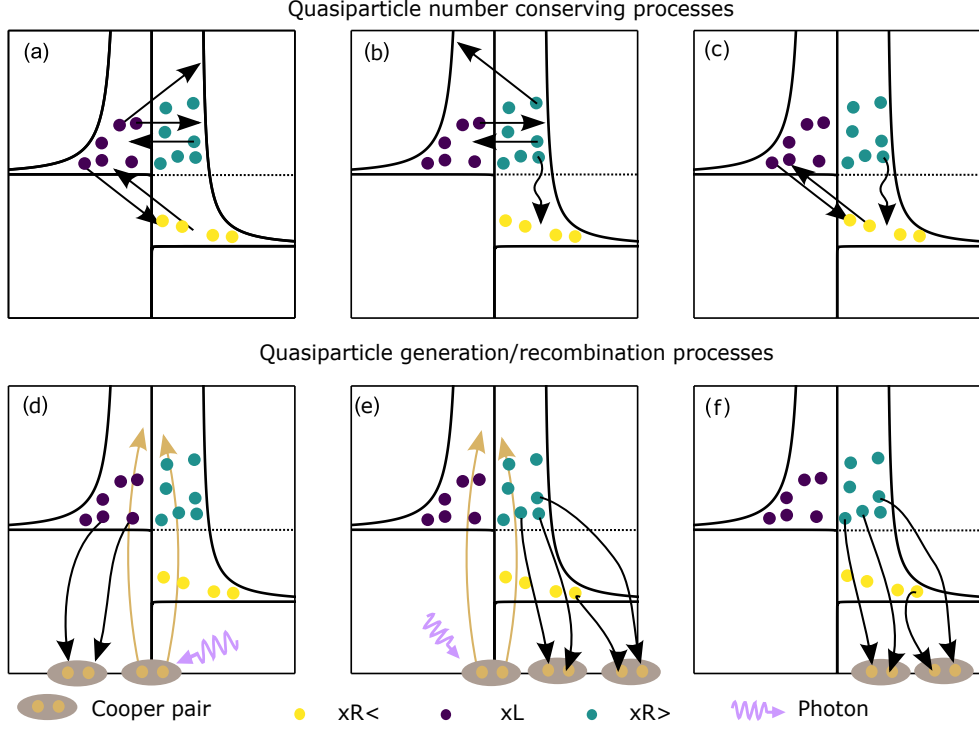


FIG. 3. Representations of the processes involving quasiparticles. Top row: processes conserving the total quasiparticle number entering the equations for (a) x_L [Eq. (11)], (b) $x_{R>}$ [Eq. (12)], and (c) $x_{R<}$ [Eq. (13)]. Horizontal arrows depict parity switching transitions, upward diagonal arrows qubit relaxation, and downward diagonal arrows qubit excitation; the downward vertical wavy arrows account for quasiparticle relaxation by phonon emission. Bottom row: processes associated with generation (upward arrows) due to pair-breaking photons (wavy arrows) or recombination (downward arrows) of quasiparticles entering the equations for (d) x_L , (e) $x_{R>}$, and (f) $x_{R<}$.

where g^α and r^α denotes quasiparticle generation and recombination rates, respectively. These equations are obtained through energy integration of the kinetic equations for the quasiparticle distribution functions $f_\alpha(\xi^\alpha)$. The terms linear in the densities account for removal/addition of single quasiparticles from/to a given electrode due to tunneling to/from the other electrode, except for the terms proportional to τ_R^{-1} which describe relaxation in the right electrode from energies above Δ_L to below it by phonon emission (see Appendix B 3). To convert the qubit transition rates $\tilde{\Gamma}_{ii'}^\alpha$ into quasiparticle rates for the (normalized) densities x_α , we find it convenient to divide those rates by a factor proportional to the number of Cooper pairs in the electrodes; concretely, we divide them by the product of volume \mathcal{V}_α times the Cooper pair density in the right electrode $n_{\text{CpR}} = 2\nu_0\Delta_R$. Therefore, the barred rates are defined as $\bar{\Gamma}_{ii'}^\alpha = \tilde{\Gamma}_{ii'}^\alpha / (2\nu_0\Delta_R\mathcal{V}_\alpha)$; for simplicity, we assume hereafter $\mathcal{V}_L = \mathcal{V}_R$. Note that some terms, namely $\bar{\Gamma}_{01}^{R<}$, $\bar{\Gamma}_{01}^{R>}$, and $\bar{\Gamma}_{00}^{R<}$, do not appear in the equations. Indeed, the rates $\bar{\Gamma}_{01}^{R<}$ and $\bar{\Gamma}_{00}^{R<}$ are exactly zero, since there are no states in the left electrode at energies smaller than Δ_L . In contrast, the term $\bar{\Gamma}_{01}^{R>}$ is neglected based on the assumption $T_{\text{qp}} \ll \omega_{10}$, which implies that there are essentially no quasiparticles with sufficient energy (that is, energy $> \Delta_L + \omega_{10}$) to make

the transition possible. A schematic representation of the various terms on the right-hand sides of Eqs. (11)-(13) is given in Fig. 3.

We remind that in writing Eqs. (11)-(13) we assumed $T_{\text{qp}} \ll \Delta_L - \Delta_R, \omega_{10}, |\Delta_L - \Delta_R - \omega_{10}|$, see the end of Sec. II. Under these assumptions, the rates $\bar{\Gamma}_{ii'}^\alpha$ are proportional to the junction conductance g_T and, with one exception, are functions of the gaps (Δ_L, Δ_R) and the qubit frequency (ω_{10}), but not of T_{qp} . The exception is the rate $\bar{\Gamma}_{00}^{R>}$, which is proportional to $\sqrt{(\Delta_L - \Delta_R)/T_{\text{qp}}}$. In experiments, typical base fridge temperatures are in the range 10-20 mK, while chip and/or effective qubit temperatures are estimated to be of order 35-60 mK, see for instance [36, 37]; given the weak dependence of only one of the rates on T_{qp} , using either fridge or effective temperature will not significantly impact the results. As an example, we plot in Fig. 4 estimates for the rates that do not change the total number of quasiparticles (cf. top row in Fig. 3), using parameters obtained from a particular experiment to be discussed in more detail in Sec. IV A. For the temperature-dependent rate $\bar{\Gamma}_{00}^{R>}$, we show with the shaded area the range of values corresponding to temperatures between 10 and 60 mK. For aluminum devices, we expect the plotted estimates to be reasonably representative: the relaxation rate τ_R^{-1}

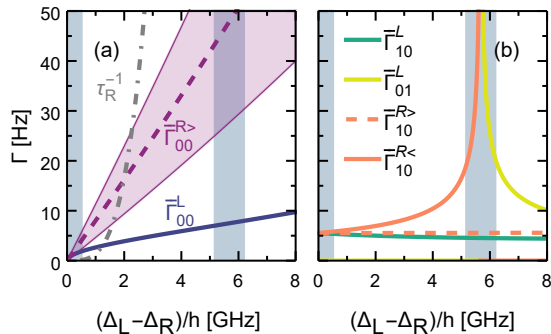


FIG. 4. Quasiparticle number conserving rates for a single junction transmon vs gaps asymmetry. (a) Quasiparticle rates for transitions that do not change the qubit logical state. The dot-dashed curve for the relaxation rate grows rapidly as $(\Delta_L - \Delta_R)^{7/2}$ (see Appendix B3). (b) Quasiparticle rates for transition changing the logical state of the qubit. Analytical expressions for the plotted rates can be found in Appendix B2. In both panels, the vertical grey shadings identify the regions outside the model applicability. Parameters: $\Delta_L/h = 52$ GHz, $\omega_{10} = 2\pi \cdot 5.7$ GHz, $E_J/h = 15.5$ GHz, $E_C/h = 290$ MHz, $\mathcal{V}_L = \mathcal{V}_R = 940 \mu\text{m}^3$, $r^L = r^{R<} = (160 \text{ ns})^{-1}$, and $\nu_0 = 0.73 \times 10^{47} \text{J}^{-1} \text{m}^{-3}$. For the dashed line in the left panel, we also set $T_{\text{qp}} = 20$ mK, while the shaded region corresponds to temperatures between 10 and 60 mK.

is material-specific, while the main factors affecting the rates $\bar{\Gamma}_{ii'}^\alpha$ are the electrode volumes and, for $i' \neq i$, the ratio E_J/E_C . Thus rates $\bar{\Gamma}_{ii'}^\alpha$ can be up to an order of magnitude slower for transmons with large electrodes (typical area $250 \times 500 \mu\text{m}^2$ [38]) and E_J/E_C up to 100, or an order of magnitude faster for transmons with small electrodes (area $80 \times 35 \mu\text{m}^2$ [39]) and E_J/E_C as low as 15.

Quasiparticle generation may be caused by pair-breaking due to both photon-assisted tunneling [34] and bulk mechanisms, $g^\alpha = g^{\alpha,ph} + g^{\alpha,b}$. The bulk generation rate can receive contributions from both photons and phonons of energy larger than $2\Delta_\alpha$, while the photon-assisted tunneling from photons of energy larger than $\Delta_L + \Delta_R$; since the junction has much higher impedance than the bulk, we expect that pair-breaking photons are primarily absorbed at the junction. As for pair-breaking phonons, recent works show that they can be generated in the substrate by absorption of environmental radiation [5, 9, 40–43]; while these non-equilibrium phonons can lead to temporary increases in the densities, the rate at which large increases happen is low ($\lesssim 0.1$ Hz), and can be further suppressed using phonon traps [44, 45], so for simplicity we neglect the bulk mechanisms, $g^{\alpha,b} = 0$.

Turning to the photon-assisted tunneling generation, the total rate at which quasiparticles are added to left electrode is $(\Gamma_{10}^{ph} + \Gamma_{11}^{ph})p_1 + (\Gamma_{01}^{ph} + \Gamma_{00}^{ph})p_0$; in the transmon regime, assuming that the photon energy is much larger than $\Delta_L + \Delta_R + \omega_{10}$ we have $\Gamma_{01}^{ph} \simeq \Gamma_{10}^{ph} \equiv \Gamma^{ph}$

and $\Gamma_{11}^{ph} \simeq \Gamma_{00}^{ph} \approx \Gamma^{ph} \sqrt{8E_J/E_C}$ [34], so that the total rate in each lead is approximately $\Gamma^{ph} (1 + \sqrt{8E_J/E_C})$. To convert this rate into a generation rate for the (normalized) density we divide it by $2\nu_0 \Delta_L \mathcal{V}_L$,

$$g^L = \frac{\Gamma^{ph}}{2\nu_0 \Delta_L \mathcal{V}_L} \left(1 + \sqrt{\frac{8E_J}{E_C}} \right). \quad (14)$$

For the generation in the right electrode, we distinguish two possibilities: first, if the photon energy is large compared to $\Delta_L + \Delta_R + \omega_{10}$, we can neglect the generation rate at energies between Δ_R and Δ_L compared to that at energies above Δ_L and set $g^{R<} = 0$, see Appendix B4; then, assuming equal volumes ($\mathcal{V}_R = \mathcal{V}_L$), we have $g^{R>} = g^L/\delta$. This first possibility is supported by the analysis [34] of experimental measurements [33]. We can similarly neglect $g^{R<}$ if thermal photons of temperature T_{ph} reach the device from higher temperature stages of the fridge, so that T_{ph} is large compared to ω_{10} and $\Delta_L - \Delta_R$ (but still smaller than Δ_R); then we find $\Gamma_{11}^{ph} \simeq \Gamma_{00}^{ph} \approx \Gamma^{ph} T_{ph} (\Delta_L + \Delta_R) / (4\Delta_L \Delta_R) \sqrt{8E_J/E_C}$ and, consequently, one should replace the terms in brackets in Eq. (14) with $1 + T_{ph} (\Delta_L + \Delta_R) / (4\Delta_L \Delta_R) \sqrt{8E_J/E_C}$. Note that although the relationships between the rates are different, the structure of the equations remains the same as for photons of large energy.

A second possibility is that the photon energy is smaller than $2\Delta_L - \omega_{10}$; then by energy conservation we have $g^{R>} = 0$; however, the relationships between the various rates $\Gamma_{ii'}^{ph}$, and therefore the expressions for the generation rates g^L and $g^{R<}$, depend on the actual value of the energy. For instance, for thermal photons with $T_{ph} \ll \omega_{10}$, $\Delta_L - \Delta_R$, we have $\Gamma_{01}^{ph} / \Gamma_{10}^{ph} = e^{-2\omega_{10}/T_{ph}}$ [34]. A detailed study of this second possibility is beyond the scope of the present work, and we focus henceforth on the situation captured by Eq. (14).

IV. STEADY STATE

Here we focus on the steady state of the quasiparticle-qubit system, obtained by setting to zero the left-hand sides of Eqs. (9), (11)-(13). We start with some considerations regarding the steady-state population of the excited state of the qubit p_1 , as they will enable us make substantial simplifications. Using $p_0 = 1 - p_1$, the population p_1 can be formally written as

$$p_1 = \frac{\Gamma_{01}^{ee} + \Gamma_{01}^{eo}}{\Gamma_{01}^{ee} + \Gamma_{01}^{eo} + \Gamma_{10}^{ee} + \Gamma_{10}^{eo}}. \quad (15)$$

As remarked in the previous section, parity-conserving rates are of non-quasiparticle origin and usually associated to a “cold” environment [33], resulting in $\Gamma_{01}^{ee} \ll \Gamma_{10}^{ee}$. For small quasiparticle densities, we expect the rates proportional to x_α to be small compared to the corresponding rates due to photon pair-breaking (that is,

$\Gamma_{ii}^{eo} \simeq \Gamma^{ph}$), so that

$$p_1 \simeq \frac{\Gamma^{ph} + \Gamma_{01}^{ee}}{\Gamma_{10}^{ee} + 2\Gamma^{ph}}. \quad (16)$$

According to recent experiments on state-of-the-art transmons [9, 33, 46, 47], the main qubit relaxation mechanism is of non-quasiparticle origin, $\Gamma_{10}^{ee} > \Gamma_{10}^{eo} \sim \Gamma^{ph}$. Indeed, in state-of-the-art qubits, the relaxation time $T_1 = (\Gamma_{10}^{ee} + \Gamma_{10}^{eo} + \Gamma_{01}^{ee} + \Gamma_{01}^{eo})^{-1}$ is of the order of few hundred μs , hence $\Gamma_{10}^{ee} \sim T_1^{-1}$ is a few kHz [9, 10, 46]. On the other hand, recent measurements reports Γ^{ph} ranging from 100 Hz down to less than 1 Hz, so that we can assume $\Gamma^{ph} \ll \Gamma_{10}^{ee}$ and $p_1 \ll 1$. Thus, well-shielded transmons are ‘‘cold’’ [36]. One can then take p_1 as a small parameter in solving the rate equations in the steady-state, and look for the zeroth-order solution by setting $p_1 = 0$ and $p_0 = 1 - p_1 = 1$. In this limit, the steady-state equations for x_α are

$$0 = g - \delta^{-1} r^L x_L^2 - (\bar{\Gamma}_{00}^L + \bar{\Gamma}_{01}^L) x_L + \bar{\Gamma}_{00}^{R>} x_{R>} \quad (17)$$

$$0 = g - r^{R>} x_{R>}^2 - (\bar{\Gamma}_{00}^{R>} + \tau_R^{-1}) x_{R>} + \bar{\Gamma}_{00}^L x_L - r^{<>} x_{R<} x_{R>} \quad (18)$$

$$0 = -r^{R<} x_{R<}^2 - r^{<>} x_{R<} x_{R>} + \tau_R^{-1} x_{R>} + \bar{\Gamma}_{01}^L x_L \quad (19)$$

where, as discussed above, we neglect generation in the right electrode at energy below Δ_L , assume equal volume electrodes, and set $g = g^{R>}$. Summation of Eqs. (17)-(19) yields the relation

$$\delta^{-1} r^L x_L^2 + r^{R>} x_{R>}^2 + r^{R<} x_{R<}^2 + 2r^{<>} x_{R<} x_{R>} = 2g, \quad (20)$$

which in fact holds for generic values of p_0, p_1 in the steady state, showing that quasiparticle generation is balanced by the recombination processes.

Before proceeding further with the study of the steady state, we note that for transmons setting $p_1 = 0$ will give more accurate results than one might naively expect. The reason is the following: consider terms of the form $\bar{\Gamma}_{00}^\alpha p_0 + \bar{\Gamma}_{11}^\alpha p_1 = \bar{\Gamma}_{00}^\alpha + (\bar{\Gamma}_{11}^\alpha - \bar{\Gamma}_{00}^\alpha) p_1$; the prefactor of the p_1 term is small compared to $\bar{\Gamma}_{00}^\alpha$ by the factor $(E_C/8E_J)^{1/2} \ll 1$, since this parameter determines the difference between the matrix elements of the parity switching transitions in the two logical states, see Appendix A (in other words, $\bar{\Gamma}_{11}^\alpha \approx \bar{\Gamma}_{00}^\alpha$). Thus, there are less conditions to be met for neglecting p_1 terms than one may guess by simply looking at the form of Eqs. (11)-(13).

A. Small gap asymmetry and comparison with experiment

We start the discussion of the qubit-quasiparticle steady state for a qubit of frequency larger than gap difference (case II). This situation is likely the most representative in experiments with transmon qubits, with typical frequency $\omega_{10}/(2\pi) \simeq 6$ GHz, and an estimated gap

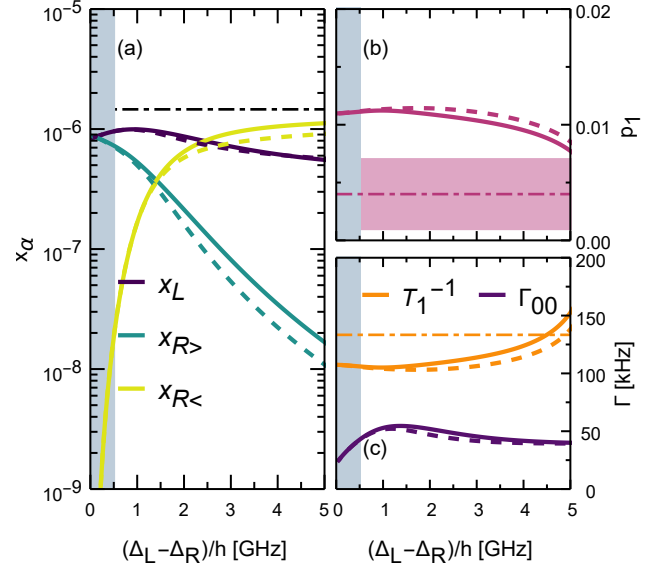


FIG. 5. Steady state for the quasiparticle-qubit system as a function of the gap difference $(\Delta_L - \Delta_R)/h$ in the modeling of the experiment of Ref. 48, whose results are represented by the horizontal dot-dashed lines. (a) Quasiparticle densities in the steady state. (b) Population of the excited state of the qubit in the steady state. (c) Qubit inverse relaxation time and parity switching rates in the steady state. The dashed curves are given by Eqs. (21)-(23) for panel (a), Eq. (24) for panel (b), and Eqs. (10) and (25) for panel (c). Parameters: $\Delta_L/h = 52$ GHz, $\omega_{10} = 2\pi \cdot 5.7$ GHz, $E_J/h = 15.5$ GHz, $E_C/h = 290$ MHz, $T_{\text{qp}} = 20$ mK, $\nu_0 = 0.73 \cdot 10^{47} \text{ J}^{-1} \text{ m}^{-3}$, $\mathcal{V}_L = \mathcal{V}_R = 940 \mu\text{m}^3$, $r^L = r^{R<} = (160 \text{ ns})^{-1}$, $\Gamma_{\text{ex}} = (16 \mu\text{s})^{-1}$.

asymmetry smaller than 5 GHz. In this case, the qubit cannot be excited by a quasiparticle tunneling transition originating from the left lead, $\bar{\Gamma}_{01}^L = 0$ (see also Fig. 4b) since there are no quasiparticle states available at energies $\sim \Delta_L - \omega_{10} < \Delta_R$ in the right lead. Hence, we can formally express the density $x_{R<}$ in terms of $x_{R>}$ by solving the quadratic equation Eq. (19),

$$x_{R<}^{II} = \frac{\sqrt{(r^{<>} x_{R>}^{II})^2 + 4\tau_R^{-1} r^{R<} x_{R>}^{II} - r^{<>} x_{R>}^{II}}}{2r^{R<}}, \quad (21)$$

where the superscript in x_α^{II} denotes that the given formulas apply to case II (and, in what follows, sufficiently close to the gaps having the same value, $\Delta_L \approx \Delta_R$).

For small values of the gap asymmetry $\eta \equiv 1 - \delta \ll 1$, the quasiparticle relaxation rate in the right lead τ_R^{-1} is small ($\tau_R^{-1} \propto \eta^{7/2}$, see Appendix B3 and dot-dashed curve in Fig. 4a), since quasiparticle states available for relaxation are constrained in the narrow energy window between Δ_R and Δ_L . Thus, quasiparticles generated with rate g at high energies, as in our modeling, accumulate at energies $> \Delta_L$ in the right lead and $x_{R<}$ is expected to be small compared to $x_{R>}$ [49]. In fact, in the limit $\tau_R^{-1} \rightarrow 0$ the leading order approximation

to Eq. (21) gives $x_{R<}^{II} \simeq \tau_R^{-1}/r^{<>}$, a formula valid for $x_{R<} \ll x_{R>}$ (in writing this condition we used that $r^{R<} \sim r^{<>}$, see Appendix B 3). Using this approximation in Eq. (18), we can solve for $x_{R>}$ in terms of x_L :

$$x_{R>}^{II} = \sqrt{\left(\frac{\bar{\Gamma}_{00}^{R>} + 2\tau_R^{-1}}{2r^{R>}}\right)^2 + \frac{g + \bar{\Gamma}_{00}^L x_L^{II}}{r^{R>}} - \frac{\bar{\Gamma}_{00}^{R>} + 2\tau_R^{-1}}{2r^{R>}}}. \quad (22)$$

Finally, we use Eq. (17) to compute x_L in a perturbative way in η ; that is, we write $x_L^{II} = x_L^{(0)} + x_L^{(1)}$, with $x_L^{(1)} \ll x_L^{(0)}$ for $\eta \ll 1$. At lowest order, we can neglect the last two terms in Eq. (17), since $\bar{\Gamma}_{00}^\alpha \rightarrow 0$ when $\eta \rightarrow 0$, and we find $x_L^{(0)} = \sqrt{\delta g/r^L}$ (we remind that $\bar{\Gamma}_{01}^L = 0$ in case II). Then neglecting terms quadratic in $x_L^{(1)}$ and solving for it, we finally arrive at

$$x_L^{II} = \frac{2x_L^{(0)2} r^L/\delta + \bar{\Gamma}_{00}^{R>} x_{R>}^{II}}{\bar{\Gamma}_{00}^L + 2x_L^{(0)} r^L/\delta} \quad (23)$$

where, for consistency, Eq. (22) for $x_{R>}^{II}$ should be used with the substitution $x_L^{II} \rightarrow x_L^{(0)}$. An approximate expression for the population of the excited state of the qubit can be subsequently obtained by substituting the analytical expressions Eqs. (21)-(23) into Eq. (15), reading

$$p_1^{II} = \frac{\Gamma^{ph} + \Gamma_{01}^{ee}}{2\Gamma^{ph} + \Gamma_{10}^{ee} + \Gamma_{01}^{ee} + \sum_\alpha \bar{\Gamma}_{10}^\alpha x_\alpha^{II}}. \quad (24)$$

Similarly, the parity switching, relaxation, and excitation rates (due to pair breaking plus quasiparticle tunneling) are obtained by substituting the same expressions into Eq. (10), while the qubit inverse lifetime is given by

$$T_1^{-1} = \Gamma_{10}^{ee} + \Gamma_{10}^{eo} + \Gamma_{01}^{ee} + \Gamma_{01}^{eo}. \quad (25)$$

For a concrete application, we test the model in the interpretation of the experimental results reported in Ref. 48. In the experiment, the authors injected quasiparticles in 3D-transmons devices and monitored their dynamics, reporting evidences for quasiparticle recombination effect for a specific design (type B in Ref. 48). Figure 5a displays the steady-state values of the quasiparticle densities x_α as a function of the gap difference. In the calculation, we consider a realistic value for the higher gap lead $\Delta_L/2\pi = 52$ GHz, a photon pair-breaking rate $\Gamma_{ph} = 1$ kHz (consistent with the measurements in Ref. [33], see also [32]), and the reported values of E_J , E_C , ω_{10} , $r = r^L \approx r^{R<}$ (see Appendix B 3), and Γ_{ex} [50] for the device B2 in Ref. 48. The quasiparticle densities obtained through numerical solution of Eqs. (9) and (11)-(13) (solid curves) [51] are compared to the approximate expressions Eqs. (21)-(23) (dashed curves). We observe that the analytical approximation for x_L is in good agreement with the numerical results in all the relevant range for our parameter values. The approximations for $x_{R<}$

and $x_{R>}$ correctly reproduce the trend of the numerical curves but, as expected, the quantitative agreement worsens with increasing gap difference when the two densities become comparable.

Notably, our model estimates compare favorably with the experimental measurements, especially keeping in mind that some experimental parameters are not known with high accuracy. First, the single-lead quasiparticle density $x_{qp} \simeq \max\{x_L, x_{R>}, x_{R<}\} \approx 10^{-6}$ is within a factor of less than 2 from the value extracted from the experimental data (dot-dashed black line) [52]. Moreover, the theoretical calculations appropriately capture the impact of nonequilibrium quasiparticles on the qubit. Indeed, the computed population of the qubit's excited state, displayed in Fig. 5b, is within a factor of three of the reported value $p_1 \simeq (0.4 \pm 0.3)\%$ and weakly dependent on the gap asymmetry. Finally, the computed inverse relaxation time of the qubit T_1^{-1} (solid orange) matches the experimental measurement (dot-dashed orange) for a gap asymmetry $(\Delta_L - \Delta_R)/(2\pi) \simeq 4.5$ GHz (see Fig. 5c). Over the whole range, nonequilibrium quasiparticles give a significant contribution (of order 40 to 60%) to the total relaxation rate. For completeness, we computed the total parity-switching rate $\Gamma_{11} \approx \Gamma_{00} = \Gamma^{ph} \sqrt{8E_J/E_C} + \bar{\Gamma}_{00}^L x_L + \bar{\Gamma}_{00}^{R>} x_{R>}$; again, a considerable part (45 to 60% in the region of validity of our model) of this rate originates from nonequilibrium quasiparticles. Parity switching can contribute to qubit dephasing [29]. Yet, the charge dispersion is small for the experimental parameters ($E_J/E_C \approx 50$) and the contribution to dephasing is also small: we estimate it to be of order 60 Hz. We note that the generation rate estimated in Ref. [48] is an order of magnitude larger than the one used in the plots of Fig. 5; we will comment on this point at the end of Sec. IV D, where we discuss possible trapping effects. The above results are based on setting $p_1 = 0$ when calculating the densities; sufficient conditions for the validity of this assumption are $p_1 \ll \bar{\Gamma}_{00}^L/\bar{\Gamma}_{10}^L$, $\bar{\Gamma}_{00}^{R>}/\bar{\Gamma}_{10}^{R>}$ in the equations for x_L and $x_{R>}$, and $p_1 \ll (r^{R<} x_{R<} + r^{<>} x_{R>})/\bar{\Gamma}_{10}^{R<}$ in the equation for $x_{R<}$. In the region of validity for case II, using the values plotted in Figs. 4 and 5 together with $r^{R<} \approx r^{<>} \approx (160 \text{ ns})^{-1}$, one can check that the conditions are in fact met.

B. Large gap asymmetry and state-of-the-art qubits

We now consider the situation in which the qubit frequency is smaller than the gap difference (case I), which may be relevant to low-frequency qubits and split transmons (see next section for a more detailed discussion of the latter). In this case, the strong gap asymmetry effectively traps quasiparticles in lower gap electrode at energy $\sim \Delta_R$. Indeed, quasiparticles initially located in the right lead at energy $\sim \Delta_R$ cannot tunnel into the left lead deexciting the qubit, $\bar{\Gamma}_{10}^{R<} = 0$, since $\omega_{10} < \Delta_L - \Delta_R$.

Conversely, quasiparticles initially located in the left electrode (with density x_L) can lose energy and excite the qubit ($\tilde{\Gamma}_{01}^L \neq 0$), populating low-energy states (thus increasing $x_{R<}$). Moreover, quasiparticles in the right lead with energy above Δ_L relax more rapidly with respect to the small-asymmetry case, due to an increased number of available quasiparticle states at lower energies (see Fig. 4). Thus, we expect the highest quasiparticle density in the low-energy states of the right lead, $x_{R<} \gg x_L, x_{R>}$.

In order to obtain approximate analytical formulas for the densities, we proceed as follows. We neglect recombination terms quadratic in the densities in Eqs. (17)-(18); these terms can be neglected if other outgoing (negative) terms are dominant, the conditions being $\delta^{-1}r^L x_L \ll \tilde{\Gamma}_{00}^L + \tilde{\Gamma}_{01}^L$ and $r^{R>}x_{R>} + r^{R<}x_{R<} \ll \tilde{\Gamma}_{00}^{R>} + \tau_R^{-1}$. Note that the term proportional to $r^{R<}$ in Eq. (19) cannot be neglected [53], as otherwise there would not be a quasiparticle sink and hence no steady state. With these approximations, the quasiparticle densities x_L and $x_{R>}$ are obtained by solving the linear system formed by Eqs. (17) and (18), while $x_{R<}$ is found after substituting the solution to the linear system into Eq. (19) (where the term proportional to $r^{R>}$ is neglected), or alternatively from Eq. (20) (where only the third term in the left-hand side is retained). Explicitly, we have

$$x_L^I = g \frac{2\tilde{\Gamma}_{00}^{R>} + \tau_R^{-1}}{\tilde{\Gamma}_{00}^L \tau_R^{-1} + \tilde{\Gamma}_{01}^L (\tilde{\Gamma}_{00}^{R>} + \tau_R^{-1})}, \quad (26)$$

$$x_{R>}^I = g \frac{2\tilde{\Gamma}_{00}^L + \tilde{\Gamma}_{01}^L}{\tilde{\Gamma}_{00}^L \tau_R^{-1} + \tilde{\Gamma}_{01}^L (\tilde{\Gamma}_{00}^{R>} + \tau_R^{-1})}, \quad (27)$$

$$x_{R<}^I = \sqrt{\frac{2g}{r^{R<}}}. \quad (28)$$

The superscript in x_α^I indicates that the given formulas apply not only in case I of gap asymmetry larger than qubit frequency, but more generally for all the situations where $x_{R<} \gg x_L, x_{R>}$. Correspondingly, the population of the excited state of the qubit reads

$$p_1^I = \frac{\Gamma^{ph} + \Gamma_{01}^{ee} + \tilde{\Gamma}_{01}^L x_L^I}{2\Gamma^{ph} + \Gamma_{10}^{ee} + \tilde{\Gamma}_{01}^L x_L^I + \sum_\alpha \tilde{\Gamma}_{10}^\alpha x_\alpha^I}. \quad (29)$$

Using the above results and those in the previous subsection, we now consider state-of-the-art transmon qubits. In terms of parameters, we take $\Gamma^{ph} = 10$ Hz, $\Gamma_{10}^{ee} = 3$ kHz, and the remaining parameters as in the plots of Fig. 5. The lower values of Γ^{ph} and Γ_{10}^{ee} in comparison to those used so far reflect improved filtering and device design and fabrication [39, 54, 55]. Figure 6(a) displays x_α obtained finding numerically the steady-state of Eqs. (9)-(13) (solid). The shaded areas in the plot denote the regions $|\Delta_L - \Delta_R| \lesssim T_{qp}$ and $|\Delta_L - \Delta_R - \omega_{10}| \lesssim T_{qp}$ where our model is not applicable. The analytical approximations of Eqs. (21)-(23) (dashed curves) are now reliable only for small values of the gap difference, because the crossover from $x_{R<} < x_{R>}$ to $x_{R<} > x_{R>}$

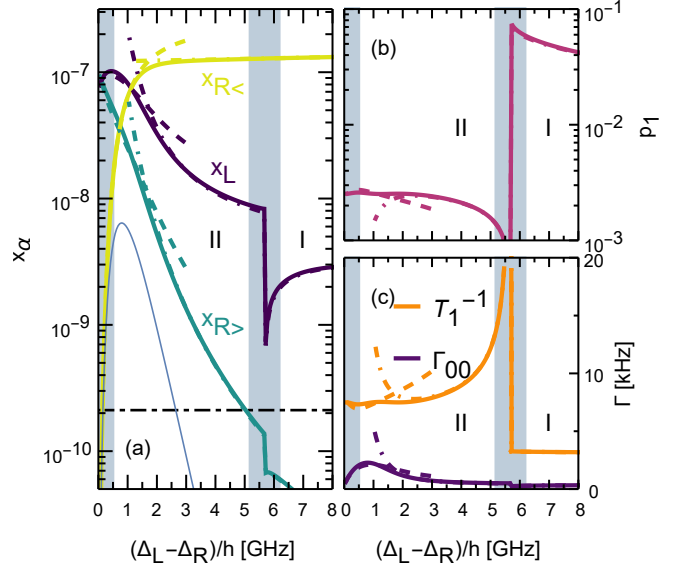


FIG. 6. Steady state for the quasiparticle-qubit system as a function of the gap difference $(\Delta_L - \Delta_R)/h$ for a state-of-the-art transmon. (a) Quasiparticle densities in the steady state. The horizontal dot-dashed line (black) denotes the quasiparticle density corresponding to a single quasiparticle. The thin blue curve shows the density $x_{R>}$ that would be expected in thermal equilibrium at temperature T_{qp} given the density $x_{R<}$. (b) Population of the excited state of the qubit in the steady-state. (c) Qubit inverse relaxation time and parity switching rate in the steady-state. In all panels, the vertical grey shadings identify the regions outside the model applicability. Parameters: $\Delta_L/h = 52$ GHz, $\omega_{10} = 2\pi \cdot 5.7$ GHz, $E_J/h = 15.5$ GHz, $E_C/h = 290$ MHz, $\Gamma^{ph} = 10$ Hz, $T_{qp} = 20$ mK, $\mathcal{V}_L = \mathcal{V}_R = 940 \mu\text{m}^3$, $r^L = r^{R<} = (160 \text{ ns})^{-1}$, $\nu_0 = 0.73 \times 10^{47} \text{J}^{-1} \text{m}^{-3}$, $\Gamma_{10}^{ee} = 3$ kHz, $\Gamma_{01}^{ee} = 0.003 \Gamma_{10}^{ee}$. The dashed curves are given by Eqs. (21)-(23) for panel (a) and Eq. (24) for panel (b), while the dot-dashed curves by Eqs. (26)-(28) for panel (a) and Eq. (29) for panel (b). In panel (c), the dashed [dot-dashed] curves are found using Eqs. (21)-(23) [(26)-(28)] in Eqs. (10) and (25).

takes place at a lower gap difference than in Fig. 5 due to the smaller generation rate. On other hand, the approximate expressions of Eqs. (26)-(28) (dotted-dashed curves) show excellent agreement with the numerical results starting from $(\Delta_L - \Delta_R)/h \approx 2$ GHz. Noting that as the asymmetry increases the relaxation rate becomes quickly the dominant one, see Fig. 4a, we can further approximate Eqs. (26) and (27) as $x_L^I \approx g/(\tilde{\Gamma}_{00}^L + \tilde{\Gamma}_{01}^L)$ and $x_{R>}^I \approx g\tau_R(2\tilde{\Gamma}_{00}^L + \tilde{\Gamma}_{01}^L)/(\tilde{\Gamma}_{00}^L + \tilde{\Gamma}_{01}^L)$; these formulas account for the jump in the densities when the gap asymmetry becomes larger than the qubit frequency, and for the fact that x_L increases after the jump.

At low generation rate, the gap difference has a stronger impact on the quasiparticle populations than in the high-generation case: already at moderate values of gap difference almost all the quasiparticles are trapped in the lower gap electrode, and the densities x_L and $x_{R>}$ are significantly smaller than $x_{R<}$, with $x_{R>} \ll x_L \ll x_{R<}$.

Interestingly, the ratio $x_{R>}/x_{R<}$ strongly deviates from the Boltzmann factor $e^{-(\Delta_L - \Delta_R)/T_{\text{qp}}}$ expected in thermal equilibrium (see thin blue curve in Fig. 6a): in the right lead there are more quasiparticles than expected at energies above Δ_L . This feature is a clear signature of large deviations from equilibrium. However, as temperature increases the relative excess in $x_{R>}$ decreases because $\bar{\Gamma}_{00}^{R>}$ is correspondingly reduced, see Fig. 4. Therefore, at these higher temperatures, it is more appropriate to assume the quasiparticle distribution to be of thermal (quasi)equilibrium form, $f_{L,R} = 1/[e^{(\epsilon - \mu_{L,R})/T_{\text{qp}}} + 1]$ with effective chemical potentials $\mu_{L,R}$, rather than treat separately $x_{R>}$ and $x_{R<}$. In a physical sense, we cannot neglect the thermal excitation of quasiparticles back to higher energies by phonon absorption. For the parameters in Fig. 6, the switch between the two approaches would take place at around 35 mK, and for the higher generation rate of Fig. 5 at around 60 mK (or even higher temperature for gap difference below about 3 GHz).

A second signature of the non-equilibrium state of the system comes from converting the qubit excited state population into an effective qubit temperature T_q via $p_1/p_0 = e^{-\omega_{10}/T_q}$. Concerning the state-of-the-art transmon (see Fig. 6b), the qubit temperature is about 44 mK at small gap difference and 86 mK for the largest difference, while for the calculations of the experiment of Ref. [48] (see Fig. 5b), we find $T_q \approx 59$ mK (for a population $p_1 \sim 1\%$). We stress that, in all cases, the effective qubit temperature is significantly larger than the quasiparticle temperature $T_{\text{qp}} = 20$ mK used in the calculations. Therefore, in general the qubit effective temperature, T_q , is not a reliable proxy for the quasiparticle one, T_{qp} .

We now consider the impact of nonequilibrium quasiparticles on experimentally measurable quantities. First, we compute the excited state population of the qubit p_1 (see Fig. 6b). We note that the population of the excited state p_1 is typically much larger in case I than in case II. This behaviour is due to two combined effects: 1) qubit excitation by quasiparticle tunneling from the left electrode at rate $\bar{\Gamma}_{01}^L x_L$ is possible in case I but suppressed in case II, 2) qubit relaxation rates associated with the low-energy quasiparticles $\bar{\Gamma}_{10}^{R<} x_{R<}$ are present only in case II. This interpretation is supported by the evolution of the relevant rates, visualized in Fig. 6(c). More precisely, in case II (left side of the panel) nonequilibrium quasiparticle tunneling gives a sizable contribution to both the qubit relaxation rate $\Gamma_{10}^{ne} = \bar{\Gamma}_{10}^L x_L + \bar{\Gamma}_{10}^{R>} x_{R>} + \bar{\Gamma}_{10}^{R<} x_{R<} \approx 4.5$ kHz [for $(\Delta_L - \Delta_R)/h \lesssim 2.5$ GHz] and to the parity switching rate, $\Gamma_{00}^{ne} = \bar{\Gamma}_{00}^L x_L + \bar{\Gamma}_{00}^{R>} x_{R>}$ in the range 0.3 – 2 kHz [where the maximum is reached for $(\Delta_L - \Delta_R)/h \sim 0.8$ GHz], larger than the contribution due to pair-breaking photons $\Gamma^{ph} \sqrt{8E_J/E_C} \simeq 200$ Hz. In case I instead (right side of the panel), the parity switching rates are almost entirely determined by the photon-assisted transitions, and the relaxation rates is mostly of nonquasiparticle nature, $\Gamma_{10} \simeq \Gamma_{10}^{ee}$.

Comparing panels (c) in Figs. 5 and 6, it is evident that the combined effect of lower Γ_{10}^{ee} and Γ^{ph} is to substantially reduce both relaxation and parity switching rates. Clearly, the reduction of the relaxation rate is advantageous; conversely, the reduction of the parity switching rate leads to an increased contribution to pure dephasing. For parity switching faster than the charge dispersion, a phenomenon analogous to ‘‘motional narrowing’’ leads to a small dephasing rate (see the end of Sec. IV A); on the contrary, we now find that parity switching is slower than the charge dispersion, so that the parity switching rate itself contributes to pure dephasing [29], thus limiting the pure dephasing time to be of order 1 ms. For gap asymmetry larger than qubit frequency, the nonequilibrium quasiparticle contribution to the rates is suppressed but, as discussed above, this come at the price of higher residual population in the qubit excited state.

C. Steady state for the stabilized qubit

Having discussed the steady-state of the quasiparticle-qubit system and analyzed the potential impact on the performance of the qubit, we now consider if the manipulation of the qubit state can be exploited to control the quasiparticle densities x_α . More precisely, we analyze the stationary values of x_α for a qubit which is continuously stabilized either in the excited state (with $p_1 \approx 1$ and $p_0 \approx 0$) or the ground state (with $p_1 \approx 0$ and $p_0 \approx 1$). Such a stabilization protocol has been recently experimentally demonstrated in a fluxonium qubit [56], yielding information on the two-level systems coupled to the qubit. For ground-state stabilization, we can still use the results for the steady state, since they were found neglecting $p_1 \ll 1$.

In the case of the qubit stabilized in the excited state, the steady-state equations for x_α are

$$0 = g - \delta^{-1} r^L x_L^2 - (\bar{\Gamma}_{11}^L + \bar{\Gamma}_{10}^L) x_L + \bar{\Gamma}_{10}^{R<} x_{R<} + (\bar{\Gamma}_{11}^{R>} + \bar{\Gamma}_{10}^{R>}) x_{R>} \quad (30)$$

$$0 = g - r^{R>} x_{R>}^2 - r^{<>} x_{R<} x_{R>} + (\bar{\Gamma}_{11}^L + \bar{\Gamma}_{10}^L) x_L - (\bar{\Gamma}_{10}^{R>} + \bar{\Gamma}_{11}^{R>} + \tau_R^{-1}) x_{R>} \quad (31)$$

$$0 = -r^{R<} x_{R<}^2 - r^{<>} x_{R<} x_{R>} + \tau_R^{-1} x_{R>} - \bar{\Gamma}_{10}^{R<} x_{R<} \quad (32)$$

The density $x_{R<}$ can be expressed in terms of $x_{R>}$ as in Eq. (21) after the substitution $r^{<>} x_{R>} \rightarrow r^{<>} x_{R>} + \bar{\Gamma}_{10}^{R<}$. To find approximate solutions for the other two densities, one could proceed similarly to Sec. IV A for small gap asymmetry (case II), and to Sec. IV B for large gap asymmetry (case I). In case II, the treatment is partially complicated by the presence of the terms proportional to $\bar{\Gamma}_{10}^{R<}$, which couple Eqs. (30) and (32). However, the rates $\bar{\Gamma}_{10}^{R<}$ and τ_R^{-1} can become dominant when increasing the gap asymmetry (see Fig. 4); this justifies dropping the terms quadratic in the densities from Eq. (32) under the condition $r^{R<} x_{R<} + r^{<>} x_{R>} \ll \bar{\Gamma}_{10}^{R<}$,

giving immediately

$$x_{R<}^{II,exc} = \frac{\tau_R^{-1}}{\bar{\Gamma}_{10}^{R<}} x_{R>}^{II,exc}, \quad (33)$$

which implies $x_{R>}^{II,exc} \ll x_{R<}^{II,exc}$. Then the term proportional to $x_{R>}^2$ can be neglected in Eq. (31) (and so the term $x_{R<}x_{R>}$ for consistency), yielding the expressions for the densities x_L and $x_{R>}$

$$x_L^{II,exc} = \sqrt{\frac{\delta g}{r^L}} \quad (34)$$

$$x_{R>}^{II,exc} = \frac{g + (\bar{\Gamma}_{11}^L + \bar{\Gamma}_{10}^L)x_L^{II,exc}}{\bar{\Gamma}_{10}^{R>} + \bar{\Gamma}_{11}^{R>} + \tau_R^{-1}} \quad (35)$$

Turning to case I, we now have $\bar{\Gamma}_{10}^{R<} = 0$. Repeating the analysis done for the non-stabilized steady state, we neglect all the recombination terms in Eqs. (30) and (31) and keep the term $r^{R<}x_{R<}^2$ in Eq. (32). Within this approximation, we retrieve Eq. (28) for $x_{R<}$, and find

$$x_L^{I,exc} = \frac{2g}{\tau_R^{-1}} \frac{\bar{\Gamma}_{11}^{R>} + \bar{\Gamma}_{10}^{R>} + \tau_R^{-1}/2}{\bar{\Gamma}_{11}^L + \bar{\Gamma}_{10}^L} \quad (36)$$

$$x_{R>}^{I,exc} = \frac{2g}{\tau_R^{-1}} \quad (37)$$

Figure 7 displays the steady-state values of the quasiparticle densities for a qubit stabilized in the logical state 0 (Fig. 7 a) and 1 (Fig. 7 b) for the same parameter values as in Fig. 6. For ground-state stabilization, the densities are approximately equal to the steady-state case, where the values of p_1 obtained through the solution of the full system are typically low (of a few percent). The stabilization in the excited state has very little effect in case I, where the term $\bar{\Gamma}_{10}^{R<}$ is suppressed. In case II, stabilization is more effective. Indeed, while $x_{R<}$ is only slightly reduced, the quasiparticle densities x_L and $x_{R>}$ are increased up to an order of magnitude compared to the small p_1 regime for gap asymmetries $\Delta_L - \Delta_R \sim 4\text{GHz}$ close to the transition to case I. This relatively large effect is seemingly in contrast with the expectation that qubit transitions are not effective at heating quasiparticles in devices with large electrodes [57]. However, the analysis in Ref. 57 assumed equal gaps, and in the nearly symmetric case we also find negligible effect. Indeed, the enhanced influence of the qubit on the quasiparticles with increasing gap difference is a consequence of the growth of the rate $\bar{\Gamma}_{10}^{R<}$, see Fig. 4. Future studies of the qubit-quasiparticle dynamics accounting for gap asymmetry may prove enlightening.

D. Trapping effects

So far, in our model for the quasiparticle dynamics we have included recombination within each electrode, but not the possible trapping of quasiparticles that can block

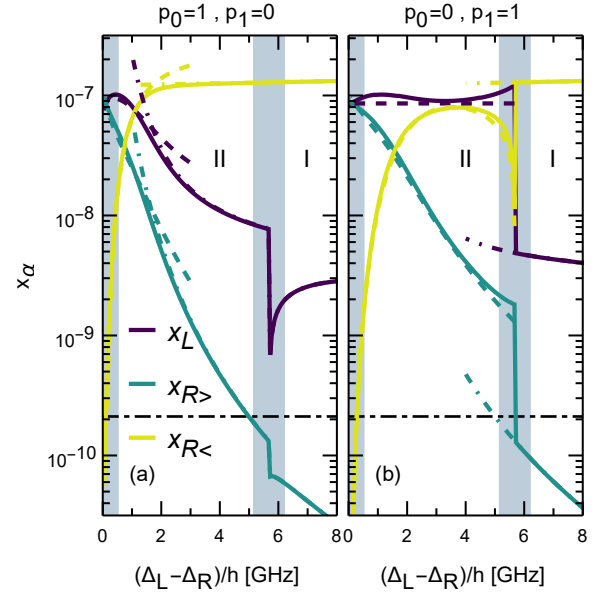


FIG. 7. Quasiparticle densities in the steady state vs gap difference $(\Delta_L - \Delta_R)/h$ for a qubit stabilized in the (a) ground state ($p_1 = 0$) or (b) excited state ($p_1 = 1$). Each horizontal dotted-dashed line identifies the density corresponding to a single quasiparticle. Parameters: $\Delta_L/h = 52\text{ GHz}$, $\omega_{10} = 2\pi \cdot 5.7\text{ GHz}$, $E_J/h = 15.5\text{ GHz}$, $E_C/h = 290\text{ MHz}$, $\Gamma^{ph} = 10\text{ Hz}$, $T_{qp} = 20\text{ mK}$, $\mathcal{V}_L = \mathcal{V}_R = 940\text{ }\mu\text{m}^3$, $r^L = r^{R<} = (160\text{ ns})^{-1}$, $\nu_0 = 0.73 \times 10^{47}\text{ J}^{-1}\text{m}^{-3}$. Dashed and dot-dashed curves in panel (a) are obtained as in Fig. 6a. In panel (b), the dashed [dot-dashed] curves are given by Eqs. (33)-(35) [(28),(36)-(37)].

them from tunneling through the junction and hence interacting with the qubit. There are two possible types of trapping, as identified in Ref. [48], background and due to vortices; the latter can be absent if the qubit is well shielded from ambient magnetic field. As for background trapping, it can at least in part be ascribed again to the gap difference in films of different thickness: away from the junction region, the two films again overlap, forming an electrode-wide junction in each electrode (see the schematic representation in Fig. 8). Therefore the right electrode of gap Δ_R is in contact with a film with gap $\Delta_L > \Delta_R$; however, this does not affect the dynamics of the densities $x_{R<}$ and $x_{R>}$. Indeed, for $x_{R<}$ the second film does not introduce new states that the quasiparticle could occupy; for $x_{R>}$, the quasiparticle can tunnel into the second film, but then they can only tunnel back, and since tunneling is fast compared to relaxation in the lower-gap film [58], the dynamics is unchanged. For the left electrode with gap Δ_L , the situation is quite different: the quasiparticles that tunnel into the second film, which now has the lower gap Δ_R , can relax by emitting phonons; those quasiparticle do not interact with the qubit, so (at low temperature $T_{qp} \ll \Delta_L - \Delta_R$ [59]) there is no mechanism for them to return to energy above Δ_L , leading to their being trapped in the second

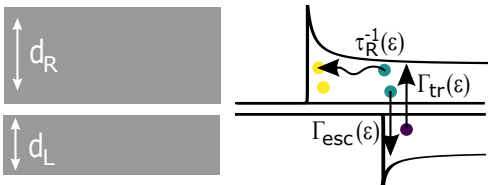


FIG. 8. Left: Schematic of the typical superconducting bilayer away from the Josephson junction region. The first film is coupled to a second film (both in gray) by a large-area insulating barrier (white). Right: Quasiparticle band diagram for the two thin aluminum films. Quasiparticles in the higher gap electrode can tunnel into the lower-gap electrode at rate $\Gamma_{tr}(\epsilon)$. In the top film, quasiparticles can relax to lower energies at rate τ_R^{-1} or tunnel back at rate $\Gamma_{esc}(\epsilon)$. The three rates combine to give the effective trapping rate τ_{tr}^{-1} of Eq. (38).

film. As mentioned above, tunneling is fast compared to relaxation and therefore the latter is the bottleneck in the trapping process, as in the case of normal-metal traps [58]. Adapting the derivation of the effective trapping rate for a normal trap to the present case of two superconductors with unequal gaps (see Fig. 8), for the trapping rate τ_{tr}^{-1} of the quasiparticles in the left electrode we find

$$\tau_{tr}^{-1} = \tau_R^{-1} \sqrt{\frac{T_{qp}}{2\Delta_L(1-\delta^2)}} \quad (38)$$

Similarly to normal traps, the effective trapping rate is smaller than the relaxation rate in the trap (here, the second superconducting film) because of the rapid escape by tunneling from the trap. More precisely, the escape is enhanced by the large final density of states $\propto (\epsilon^2 - \Delta_L^2)^{-1/2}$ in the first superconducting film at energies $\sim \Delta_L$. Note that the trapping rate vanishes in the limit of equal gaps $\delta \rightarrow 1$, due to the rapid suppression of $\tau_R^{-1} \propto (1-\delta)^{7/2}$. Interestingly, with the parameters we are employing ($\Delta_L/h = 52$ GHz, $r^L = (160 \text{ ns})^{-1}$, $T_{qp} = 20$ mK), we estimate that τ_{tr}^{-1} can reach up to about 100 Hz, and can therefore explain most if not all of the observed background trapping that ranges between 30 and 180 Hz [48]. Moreover, in the Supplementary Note 5 to Ref. [48], it was noted that measurements of the quasiparticle dynamics could be better modeled assuming background trapping to be present in only one electrode, as in the mechanism here considered.

This trapping process is accounted for by adding the term $-\tau_{tr}^{-1}x_L$ to the right-hand side of Eq. (11), which represents a sink for quasiparticles. Its qualitative effect is to lower the quasiparticle densities (at fixed values of other parameters). Indeed, for small gap asymmetry the only modification to the results presented in Sec. IV A is to add a term τ_{tr}^{-1} in the denominator in the right-hand side of Eq. (23). Therefore, at small asymmetry we expect little impact on $x_{R>}$ and $x_{R<}$, and a small decrease in x_L which becomes more pronounced

with increasing asymmetry. In fact for large asymmetry, when relaxation and trapping become dominant, i.e., $\tau_R^{-1}, \tau_{tr}^{-1} \gg \bar{\Gamma}_{00}^L, \bar{\Gamma}_{01}^L$, following the approach of Sec. IV B we find the approximate results $x_L \approx g\tau_{tr}$, $x_{R>} \approx g\tau_R$, and $x_{R<} \approx \sqrt{g/r^{R<}} \sqrt{1 + \tau_{tr}\bar{\Gamma}_{01}^L}$. In comparison to the results in the absence of trapping, these equations predict a numerical factor reduction for $x_{R>}$ and $x_{R<}$, but a strong suppression for x_L .

We have verified the above results by repeating the numerical calculations of the previous two subsections. In Fig. 5, the inclusion of trapping would give a sizable effect only for gap asymmetries larger than 2 GHz. In particular, x_L is reduced with respect to the no-trapping case up to an order of magnitude [for $(\Delta_L - \Delta_R)/h \sim 5$ GHz], while $x_{R<}$ and $x_{R>}$ are only slightly modified and still very well captured by the approximate estimates (dashed curves in Fig. 5). The impact on the experimentally measurable quantities is rather limited, and characterized by reduced rates $T_1^{-1} \approx 125$ kHz (down from 152 kHz), $\Gamma_{00} \approx 24$ kHz (down from 40 kHz), and slightly increased qubit excited state population $p_1 \approx 0.009$ (up from 0.008) at the reference value $\Delta_L - \Delta_R \sim 5$ GHz. Concerning the state-of-the-art transmon, similar conclusions on the rates and p_1 can be drawn for gap difference smaller than qubit frequency. For strongly asymmetric junctions discussed in Sec. IV B with $\Delta_L - \Delta_R > \omega_{10}$, the quasiparticle depletion in the higher-gap electrode is associated with a significant reduction of p_1 down to 1% (for $(\Delta_L - \Delta_R)/h \sim 8$ GHz), and no significant impact on the qubit rates, since even without trapping quasiparticle tunneling gives them a negligible contribution.

Trapping by vortices has qualitatively a similar effect, that of reducing all the densities. For a small number of vortices [48], vortex trapping adds a term $-N_L\tau_V^{-1}x_L$ to the right-hand side of Eq. (11), where $\tau_V^{-1} = P/A$ is the trapping rate due to a single vortex and N_L is the number of vortices in the left electrode. Here $P = 0.067 \text{ cm}^2/\text{s}$ is the vortex trapping power measured in Ref. [48], and A is the area of the electrode; for device B2 in that reference, the single-vortex trapping rate is $\tau_V^{-1} \simeq 400$ Hz. We note that this simplified approach overestimates the trapping rate, and a more accurate estimate can be obtained by taking into account the actual geometry of the device. Experimentally, the increase in the trapping rate by adding a single vortex was of the order 200 Hz, and we use this value for our estimates. Assuming that the trapping into vortices is again mediated by relaxation via phonon emission, the corresponding terms to add to the right-hand sides of Eqs. (12) and (13) are $-N_R[1 - (1-\delta)^3]\tau_V^{-1}x_{R>}$ and $-N_R\delta^3\tau_V^{-1}x_{R<}$, respectively (the cubic dependencies arise from integration over the phonon frequency of the electron-phonon matrix element, see Appendix B3). In the presence of at least one vortex in both electrodes, all the non-linear terms in Eqs. (11)-(13) can be dropped, since for typical experimental parameters $r^\alpha x_\alpha \ll \tau_V^{-1}$; the steady-state values of x_α are then obtained by solving the linear system. For x_L and $x_{R>}$, Eqs. (26)-(27) give a good approximation

after the replacements $\tau_R^{-1} \rightarrow \tau_R^{-1} + N_R[1 - (1 - \delta)^3]\tau_V^{-1}$ and $\bar{\Gamma}_{01}^L \rightarrow \bar{\Gamma}_{01}^L + N_L\tau_V^{-1}/\delta$. After these substitutions, even with a single vortex in each electrode the steady-state densities x_L and $x_{R>}$ of Fig. 5 are reduced down to about 2×10^{-8} (or even less for the latter). Similar values are found in the case of $x_{R<}$, which can be expressed as $x_{R<} = (\bar{\Gamma}_{01}^L x_L + \tau_R^{-1} x_{R>})\tau_V/N_R\delta^3$.

As consequence of the strong reduction of the densities in comparison with the estimates in Fig. 5, T_1^{-1} is reduced by approximately 30 kHz when a single vortex is included in the left electrode. Upon including an additional vortex in the right electrode, quasiparticle tunnelling would give a negligible contribution to the total relaxation and parity switching rates and to determining the qubit excited population [cf. Eq. (24)]. Our findings are in semi-quantitative agreement with the measurements on device B2 of Ref. 48, where upon the addition of a single vortex the decay rate fell by about 35 kHz, followed by another decrease after the addition of a vortex in the opposite pad, and no more changes in T_1 (within error bars) with more vortices. In contrast, device B1 showed a more gradual reduction in the relaxation rate with increasing number of vortices [48]. The inclusion of a background source of quasiparticle generation could further improve the quantitative agreement between theory and experiment, and possibly reduce the discrepancy between our estimate of the generation rate and that in Ref. 48 mentioned in Sec. IV A. A more detailed comparison with experiments is left to future studies.

In closing this section we comment briefly on the effect of vortices in qubits with large electrodes (type A devices in Ref. 48 with electrode area $A = 250 \times 500 \mu\text{m}^2$). While the single-vortex trapping rate τ_V^{-1} decreases with increasing area A , the number of vortices in the electrode for a given magnetic field increases. In fact, it is likely that several vortices are always present in large electrodes, leading to a total trapping rate in each electrode comparable to or larger than that estimated above for a single vortex. Then, based on our analysis, we expect that for values of Γ^{ph} of order 10 Hz or lower, the quasiparticle tunneling contribution to the qubit transition rates is strongly suppressed by vortex trapping. Based on the results of Refs. [58, 60], we expect this conclusion to hold also in the presence of engineered normal or superconducting traps.

V. SPLIT TRANSMON

In the previous section, we have discussed the steady-state values for the quasiparticle densities and the corresponding transition rates as a function of the gap difference $\Delta_L - \Delta_R$. In particular, we have shown that quantities of experimental interest, such as the qubit excited state population or its inverse lifetime, may be significantly different depending on whether the qubit frequency ω_{10} is greater or lower than the gap difference $\Delta_L - \Delta_R$. The gap difference is determined by the

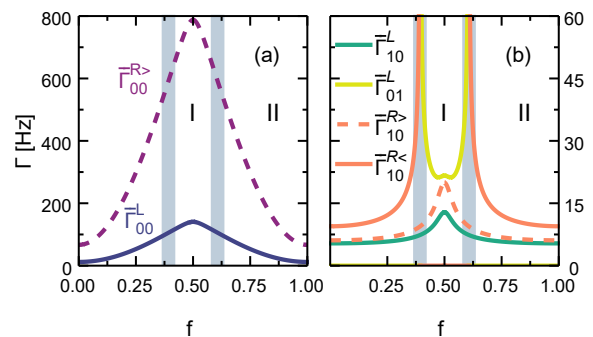


FIG. 9. Quasiparticle rates vs normalized flux in a split transmon. (a) Parity switching rates. (b) Relaxation and excitation rates. (See Appendix C 1 for analytical expressions.) The shaded regions denote the region where the model cannot be applied. Parameters: $\Delta_L/h = 52$ GHz, $\Delta_R/h = 48$ GHz, $\omega_{10}(0) = 2\pi \cdot 7$ GHz, $g_T^\Sigma = 2 \times 2.5g_K$, $\nu_0 = 0.73 \times 10^{47} \text{ J}^{-1}\text{m}^{-3}$, $\mathcal{V}_L = \mathcal{V}_R = 940 \mu\text{m}^3$, $T_{\text{qp}} = 20$ mK.

nanofabrication process, through the thickness and the resistivity of the Al thin films composing the Josephson junctions, see Sec. I. The gaps can be controlled to some extent by applying a magnetic field parallel to the films, if their thickness is at least of order 7 nm [19]; the gap difference is expected to grow as the field increases, since thinner films have higher gap and higher critical field. Although the overall suppression of the gaps also causes the qubit frequency to decrease, as confirmed in a recent experiment [61], it should be possible to engineer devices in which the sign of $\omega_{10} - (\Delta_L - \Delta_R)$ can be flipped.

Here we consider a qubit design in which the transition frequency ω_{10} can be tuned on-chip. In the split transmon, a superconducting ring interrupted by two Josephson junctions replaces the single junction, so that the Josephson energy (and thus the frequency) can be controlled by threading a magnetic flux through the loop. More precisely, the Josephson energy $E_J(f) = E_J^\Sigma |\cos(\pi f)| \sqrt{1 + d^2 \tan^2(\pi f)}$ and the qubit frequency $\omega_{10}(f) = \sqrt{8E_J(f)E_C} - E_C$ are periodic functions of the normalized magnetic flux $f = \Phi/\Phi_0$ with period one, where $\Phi_0 = h/2e$ is the flux quantum. The quantity $d = |E_J^1 - E_J^2|/E_J^\Sigma$ accounts for the asymmetry between the two junctions and express the maximum relative suppression of the Josephson energy (occurring for $f = 0.5$ modulo one) with respect to the zero-field value $E_J^\Sigma = E_J^1 + E_J^2$ – see also Appendix C.

For a split transmon, the transition rates are properly computed by summing the contributions due to quasiparticles tunneling in each junction, as discussed in detail in Ref. [27]. As a result, the rates depend on the magnetic flux f through both the frequency dependence of the spectral density [Eq. (5)] and the matrix elements in Eq. (4), see Appendix C. The qubit-quasiparticle dynamics is still described in terms of the generalized Rothwarf-Taylor equations Eqs. (11)-(13).

Figure 9 displays the flux evolution of the transi-

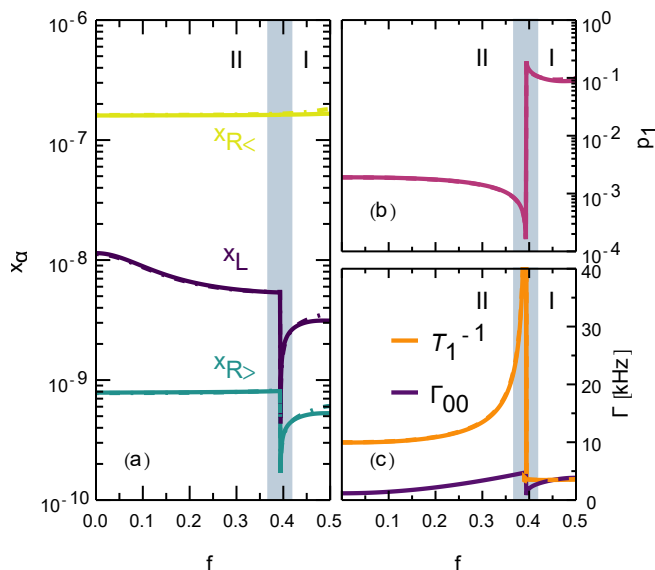


FIG. 10. Qubit-quasiparticle steady state vs normalized flux for a split transmon. (a) Quasiparticle densities in the steady state. (b) Excited state population of the qubit. (c) Qubit inverse relaxation time and parity switching rate in the steady-state. Parameters: $\Delta_L/h = 52$ GHz, $\Delta_R/h = 48$ GHz, $\omega_{10}(0) = 2\pi \cdot 7$ GHz, $g_T^\Sigma = 2 \times 2.5g_K$, $T_{\text{qp}} = 20$ mK, $\Gamma^{ph} = 10$ Hz, $\mathcal{V}_L = \mathcal{V}_R = 940 \mu\text{m}^3$, $\nu_0 = 0.73 \times 10^{47} \text{J}^{-1}\text{m}^{-3}$, $\Gamma_{10}^{ee} = 3$ kHz. The dashed lines, barely distinguishable from the solid ones, are obtained as in Fig. 6, using the expressions for case I and the flux-dependent rates of Appendix C 1.

tion rates conserving the total quasiparticle number in Eqs. (11)-(13) in a typical transmon device with $\omega_{10}(0) > \Delta_L - \Delta_R$ and focusing on a single period. The parity-switching rates, $\tilde{\Gamma}_{ii}^\alpha$, (see Fig. 9a) and the relaxation rates due to quasiparticles located at energies larger than Δ_L , $\tilde{\Gamma}_{10}^L$ and $\tilde{\Gamma}_{10}^{R>}$ (Fig. 9b), increase monotonically with f in the half-period $[0, 0.5]$. The relaxation rate associated to quasiparticle residing at energies $\sim \Delta_R$ in the right lead $\tilde{\Gamma}_{10}^{R<}$ displays a monotonic growth for fluxes up to $f = f_c \approx 0.4$, where the BCS model predicts a divergence due to the resonant condition $\omega_{10}(f_c) = \Delta_L - \Delta_R$ (we recall however that our model cannot be applied here, see shaded regions in the plot), and it is zero for fluxes closer to the half-flux quantum. Similarly, the excitation rate $\tilde{\Gamma}_{01}^L$ is finite only for values of the flux where $\omega_{10}(f) < \Delta_L - \Delta_R$, i.e., $|f - 0.5| < 0.5 - f_c$. As mentioned above, a split transmon makes it in principle possible to switch between the two regimes, which we named case II and case I in the previous sections, if $\omega_{10}(0) > \Delta_L - \Delta_R$ (case II) and $\omega_{10}(0.5) < \Delta_L - \Delta_R$ (case I).

A. Steady state

Here we briefly discuss the steady state of the qubit-quasiparticle system as a function of the magnetic flux f . We consider a split-transmon of frequency $\omega_{10}(0) =$

$2\pi \cdot 7$ GHz, gaps $\Delta_L/2\pi = 52$ GHz and $\Delta_R/2\pi = 48$ GHz, and junctions asymmetry $d = 0.1$; other parameters are as in the previous sections. Figure 10 displays (a) the steady-state values of the quasiparticle densities, (b) the population of the excited state of the qubit and (c) the qubit relaxation and parity switching rates as a function of the reduced magnetic flux. Due to the sizable gap asymmetry, quasiparticles are mostly located in the lower-gap electrode at energies $\sim \Delta_R$, in agreement with the discussion of the previous section. In particular, the density $x_{R<} \approx \sqrt{2g/r^{R<}}$ does not significantly depend on the magnetic flux, while the quasiparticle density in the left lead decreases monotonically by increasing the magnetic flux from zero up to the value f_c where the resonant condition $\omega_{10}(f_c) = \Delta_L - \Delta_R$ is met. In our modeling, the crossing of the resonant condition with flux significantly affects the population of the excited state of the qubit, which is enhanced for values of the flux where $\omega_{10}(f) < \Delta_L - \Delta_R$. However, we note that this effect may be mitigated by the presence of vortex trapping, as discussed in Sec. IV D. Similarly, the relaxation rate of the qubit is reduced for fluxes close to the half-quantum compared to fluxes such that $\omega_{10}(f) - (\Delta_L - \Delta_R) \gg T_{\text{qp}}$, and it is expected to grow as the resonance condition is approached in increasing flux due to the increase in the rate $\tilde{\Gamma}_{10}^{R<}$, cf. Fig. 9b [62] (we remind that our model cannot be quantitatively applied too close to the resonant flux value, where the condition $T_{\text{qp}} \ll |\omega_{10} - \Delta_L + \Delta_R|$ is violated). The parity switching rate is less affected by the magnetic flux, and typically increases in the range $[0, f_c]$; the dip at $f > f_c$ reflects the decrease in the density x_L , which itself is a consequence of the finite value of $\tilde{\Gamma}_{01}^L$ at those fluxes (cf. Sec. IV B).

Finally, we note that with our choice of parameters, namely photon energy large compared to $2\Delta_L$ (see Sec. III), the photon-assisted transition rate Γ^{ph} and the generation rate g depend only weakly on flux f , while a stronger dependence is expected for photons with energy closer to the threshold $\Delta_L + \Delta_R$, see Appendix C 2. Moreover, as in the case of the single-junction transmon, we expect that in the presence of vortices or engineered traps the quasiparticle densities, and hence the quasiparticle contributions to the transition rates, will be suppressed.

VI. SUMMARY AND OUTLOOK

In this work we theoretically address the intrinsic decoherence in superconducting qubits due to quasiparticles, generalizing previous investigations to take into account the finite gap difference, or gap asymmetry, between the junction leads, see Sec. II. We develop a model for the coupled qubit-quasiparticle system, where quasiparticles in each lead occupy narrow energy windows of width T_{qp} (the effective quasiparticle temperature) located just above the gaps Δ_L and Δ_R of the left and right leads. This approach aims to model the experimental evidence of excess nonequilibrium quasiparticles in superconduct-

ing qubits operating at the base temperature of dilution refrigerators; for temperature T_{qp} low compared to other energy scales (such as qubit frequency ω_{10} and gap difference $\Delta_L - \Delta_R$), the model displays a weak dependence on T_{qp} and the quasiparticles can be described in terms of nonequilibrium densities, see Sec. III. A graphic representation of the various physical processes included in the model (tunneling, relaxation, generation, and recombination) is given in Fig. 3.

In Sec. IV we discuss the steady-state values for the quasiparticle densities and their impact on the qubit, under the assumption that quasiparticle generation is dominated by pair-breaking at the junction due to the absorption of photons with energy well above the sum of the gaps. We find that the gap asymmetry can affect the qubit even if it does not impact on the total number of nonequilibrium quasiparticles in the superconducting leads, number that is determined by the balance between generation and recombination (in the absence of trapping, for instance by vortices). More precisely, the gap asymmetry affects the energy distribution of the nonequilibrium quasiparticles: for small asymmetry, the quasiparticles in both leads are located at energies close to the higher of the two gap (Δ_L in our manuscript), while they are largely “trapped” in the lead with the lower gap energy (Δ_R) for strong asymmetries.

The case of asymmetry small compared to the qubit frequency (case II in our nomenclature) is likely representative of typical transmon qubits. Since quasiparticles are present in both leads, they can tunnel in both directions and absorb energy from the qubit, causing relaxation. In this regime the qubit lifetime can be significantly affected by nonequilibrium quasiparticles, if no or limited quasiparticle trapping is present. This fact is made evident by our re-examination (Sec. IV A) of the experimental findings of Ref. 48, concerning quasiparticles either in the presence or absence of vortex trapping. Even with the improved filtering of state-of-the-art setups, which lowers the generation rate by a few orders of magnitude, a full suppression of the nonequilibrium quasiparticle effects on the qubit is possibly achieved only through additional trapping for a nearly-symmetric device (see the discussion in Sec. IV B). In contrast, for larger asymmetry, quasiparticle relaxation tends to be dominant, thus populating the states with energy close to the smaller gap Δ_R . In the case of qubit frequency smaller than gap asymmetry (case I), quasiparticles are effectively trapped and cannot tunnel to the higher-gap lead. Since a relaxation channel present in case II is not available in case I, typically the qubit lifetime improves for a given quasiparticle generation rate, but the population of the qubit excited state also increases, see Fig. 6.

While in this paper we consider for concreteness transmon qubits, our findings could be relevant to other qubit designs; for example, case I (gap asymmetry larger than qubit frequency) likely applies to low-frequency qubits, such as the fluxonium [63]. Future applications of our model could give insights into fundamental quan-

ties in the superconducting state, such as the energy-dependent relaxation rate. Indeed, we have discussed how the differences between case II (quasi-symmetric junction) and case I (strongly asymmetric junction) are related to the interplay between quasiparticle tunneling and relaxation in the lead with the smaller gap. Hence, the investigation of the dynamics after stabilization (Sec. IV C), or taking advantage of the magnetic flux control in a split transmon (Sec. V), may give information on such quantities. Our analysis also points toward the fact that the lifetime of the qubit can be severely limited when the qubit frequency is resonant with the gap difference. Therefore, from an experimental perspective, this situation should be avoided. On the theoretical side, the modeling in terms of quasiparticle densities cannot be adopted, and the predicted divergence within lowest-order perturbation theory applied to the BCS state needs to be properly renormalized, so further study of the resonant regime is needed.

ACKNOWLEDGMENTS

We acknowledge D. Spencer, V. Fatemi, M. Hayes, K. Serniak, and L. Glazman for discussions of their work [64] prior to publication. G.C. acknowledges support by the German Federal Ministry of Education and Research (BMBF), funding program “Quantum technologies – from basic research to market”, project QSolid (Grant No. 13N16149).

Appendix A: Matrix elements for single-junction transmon

We denote the transmon states as $|ij\rangle$, with $i \in \{0, 1\}$ for the logical value and $j \in \{e, o\}$ the parity. For both $\sin \hat{\varphi}/2$ and $\cos \hat{\varphi}/2$, matrix elements between states with the same parity vanish. For states of opposite parity ($\bar{e} = o$ and $\bar{o} = e$), in a single junction transmon the matrix elements associated with the transition between different qubit states are approximately [29]:

$$\langle 1j | \sin \frac{\hat{\varphi}}{2} | 0\bar{j} \rangle \simeq \left(\frac{E_C}{8E_J} \right)^{1/4}, \quad (\text{A1})$$

$$\left| \langle ij | \sin \frac{\hat{\varphi}}{2} | i\bar{j} \rangle \right| \simeq |\sin(2\pi n_g)| \left(\frac{2}{3} \right)^{\frac{2}{3}} \Gamma \left(\frac{1}{3} \right) \left(\frac{E_C}{8E_J} \right)^{\frac{1}{6}} \frac{\varepsilon_i}{\omega_p}, \quad (\text{A2})$$

$$\langle ij | \cos \frac{\hat{\varphi}}{2} | i\bar{j} \rangle \simeq 1 - \left(i + \frac{1}{2} \right) \sqrt{\frac{E_C}{8E_J}} - \frac{3}{2} \left(i + \frac{1}{4} \right) \frac{E_C}{8E_J}, \quad (\text{A3})$$

$$\left| \langle 1j | \cos \frac{\hat{\varphi}}{2} | 0\bar{j} \rangle \right| \propto |\sin(2\pi n_g)| \frac{\sqrt{|\varepsilon_0 \varepsilon_1|}}{\omega_p} \left(\frac{E_C}{E_J} \right)^{1/3}. \quad (\text{A4})$$

Here Γ denotes the gamma function and ε_i the charge dispersion of level i (that is, the energy difference between

different parities):

$$\varepsilon_i = (-1)^i E_C \sqrt{\frac{2}{\pi}} \frac{2^{2i+2}}{i!} \left(\frac{8E_J}{E_C}\right)^{(2i+3)/4} e^{-\sqrt{8E_J/E_C}} \quad (\text{A5})$$

We note that at leading order in $E_J/E_C \gg 1$ the right-hand side of Eq. (A3) is independent of i , and that due to their exponential suppression, the right-hand sides of Eqs. (A2) and (A4) can be set to zero.

Appendix B: Microscopic derivation of the transition rates

The derivation of the transition rates for a qubit interacting with a quasiparticle bath has been reported in detail before, see *e.g.* [27]. The extension to include the quasiparticle dynamics amounts to the derivation of the kinetic equation for the quasiparticle distribution function followed by integration over energy to arrive at equations for the quasiparticle densities. The quasiparticle kinetic equation has also been considered before, see *e.g.* [57] and references therein, so here we only outline the main differences with previous treatments.

1. Definitions of the densities

For the normalized density of quasiparticle in the left electrode our definition is the same as in the literature, namely

$$x_L = \frac{2}{\Delta_L} \int_{\Delta_L}^{+\infty} d\epsilon \frac{\epsilon f_L(\epsilon)}{\sqrt{\epsilon^2 - \Delta_L^2}}. \quad (\text{B1})$$

where f_L denotes the quasiparticle distribution function in the left lead.

For the right electrode we assume that, due to the competition between tunneling processes across the Josephson junction and quasiparticle relaxation in the right electrode, the distribution function f_R is the sum of two contributions with support in a narrow energy window immediately above the two gaps Δ_R and Δ_L ; the width of this energy window is what we call the effective quasiparticle temperature T_{qp} , and we assume $T_{\text{qp}} \ll \Delta_L - \Delta_R$. Therefore we write $f_R(\epsilon) = f_R^<(\epsilon)\theta(\Delta_L - \epsilon) + f_R^>(\epsilon)\theta(\epsilon - \Delta_L)$; correspondingly, we can identify two quasiparticle densities $x_{R<}$ and $x_{R>}$, where

$$x_{R<} = \frac{2}{\Delta_R} \int_{\Delta_R}^{\Delta_L} d\epsilon \frac{\epsilon f_R^<(\epsilon)}{\sqrt{\epsilon^2 - \Delta_R^2}}, \quad (\text{B2})$$

$$\begin{aligned} x_{R>} &= \frac{2}{\Delta_R} \int_{\Delta_L}^{+\infty} d\epsilon \frac{\epsilon f_R^>(\epsilon)}{\sqrt{\epsilon^2 - \Delta_R^2}} \quad (\text{B3}) \\ &\simeq \frac{2}{\Delta_R} \frac{\Delta_L}{\sqrt{\Delta_L^2 - \Delta_R^2}} \int_{\Delta_L}^{+\infty} d\epsilon f_R^>(\epsilon). \end{aligned}$$

The approximation in the last line follows from our assumption of low effective temperature compared to gap difference.

2. Transition rates for a single-junction transmon

The golden-rule formula for the qubit transition rate Γ_{if} is given in Eq. (4), with the matrix elements of Appendix A. Using the assumptions $T_{\text{qp}} \ll \Delta_L - \Delta_R$, ω_{10} , $|\Delta_L - \Delta_R - \omega_{10}|$, we can factorize the rate in the form $\Gamma_{if} = \tilde{\Gamma}_{if}^\alpha x_\alpha$. At leading order in $E_C/E_J \ll 1$, we find for the parity switching rates

$$\tilde{\Gamma}_{ii}^L \simeq \frac{gT\Delta_L}{e^2} \frac{\Delta_L - \Delta_R}{\sqrt{\Delta_L^2 - \Delta_R^2}} \quad (\text{B4})$$

$$\tilde{\Gamma}_{ii}^{R>} \simeq \frac{gT\Delta_R}{e^2} \sqrt{2} \frac{\Delta_L - \Delta_R}{\sqrt{T_{\text{qp}}\Delta_L}} \quad (\text{B5})$$

These expressions are valid for $T_{\text{qp}} \ll \Delta_L - \Delta_R$. We note that in writing $\tilde{\Gamma}_{ii}^{R>}$ we assume a constant value of $f_R^>(\epsilon)$ in the narrow support $[\Delta_L, \Delta_L + T_{\text{qp}}]$. Yet, we remark that our result is not strictly specific to this assumption and is expected to hold more generally within a numerical prefactor of order 1 (see also the discussion in Appendix A of Ref. 60). Introducing the short-hand notation $s_{10} = (E_C/8E_J)^{1/4}$, the relaxation rates are

$$\tilde{\Gamma}_{10}^L \simeq s_{10}^2 \frac{gT\Delta_L}{e^2} \frac{\Delta_L + \omega_{10} + \Delta_R}{\sqrt{(\Delta_L + \omega_{10})^2 - \Delta_R^2}} \quad (\text{B6})$$

$$\tilde{\Gamma}_{10}^{R>} \simeq s_{10}^2 \frac{gT\Delta_R}{e^2} \frac{\Delta_L + \omega_{10} + \Delta_R}{\sqrt{\omega_{10}(2\Delta_L + \omega_{10})}} \quad (\text{B7})$$

$$\tilde{\Gamma}_{10}^{R<} \simeq \begin{cases} 0 & \text{I} \\ s_{10}^2 \frac{gT\Delta_R}{e^2} \frac{\Delta_R + \omega_{10} + \Delta_L}{\sqrt{(\Delta_R + \omega_{10})^2 - \Delta_L^2}} & \text{II} \end{cases} \quad (\text{B8})$$

where I and II refer to case I, $\Delta_L - \Delta_R - \omega_{10} \gg T_{\text{qp}}$, and case II, $\omega_{10} - (\Delta_L - \Delta_R) \gg T_{\text{qp}}$, respectively (cf. Sec. II). Finally the excitation rates are

$$\tilde{\Gamma}_{01}^L \simeq \begin{cases} s_{10}^2 \frac{gT\Delta_L}{e^2} \frac{\Delta_L - \omega_{10} + \Delta_R}{\sqrt{(\Delta_L - \omega_{10})^2 - \Delta_R^2}} & \text{I} \\ 0 & \text{II} \end{cases} \quad (\text{B9})$$

$$\tilde{\Gamma}_{01}^{R>} \simeq \tilde{\Gamma}_{01}^{R<} \simeq 0 \quad (\text{B10})$$

where the last line is a consequence of the assumption $T_{\text{qp}} \ll \omega_{10}$.

3. Relaxation and recombination due to phonons

The kinetic equation for the quasiparticle distribution function accounting for electron-phonon interaction can be written in the form $df_\alpha(\epsilon)/dt = \text{St}\{f, n\}$, where the collision integral St is in general a functional of the both the quasiparticle (f) and phonon (n) distribution functions. Explicit formulas for the collision integral can be found for instance in Refs. 65 and 66. Here we assume sufficiently low (effective) temperature, so that the phonons can be treated as a cold bath, $n = 0$, and the quasiparticle occupation probability is small, $f_\alpha \ll 1$. Then the collision integral consists of three terms, $\text{St} = \text{St}_{in} - \text{St}_{out} - \text{St}_{rec}$: an incoming term St_{in}

due to relaxation of quasiparticle from higher energy, an outgoing term St_{out} due to relaxation to lower energy, and a second outgoing term St_{rec} due to the recombination of two quasiparticles into a Cooper pair. All these processes take place via phonon emission.

With our assumptions, the three collision integrals are

$$St_{in} = 2\pi \int_0^\infty d\omega F_\alpha(\omega) \frac{\epsilon(\epsilon + \omega) - \Delta_\alpha^2}{\epsilon\sqrt{(\epsilon + \omega)^2 - \Delta_\alpha^2}} f_\alpha(\epsilon + \omega) \quad (B11)$$

$$St_{out} = 2\pi \int_0^{\epsilon - \Delta_\alpha} d\omega F_\alpha(\omega) \frac{\epsilon(\epsilon - \omega) - \Delta_\alpha^2}{\epsilon\sqrt{(\epsilon - \omega)^2 - \Delta_\alpha^2}} f_\alpha(\epsilon) \quad (B12)$$

$$St_{rec} = 2\pi \int_{\epsilon + \Delta_\alpha}^\infty d\omega F_\alpha(\omega) \frac{\epsilon(\omega - \epsilon) + \Delta_\alpha^2}{\epsilon\sqrt{(\omega - \epsilon)^2 - \Delta_\alpha^2}} f_\alpha(\omega - \epsilon) f_\alpha(\epsilon) \quad (B13)$$

where the spectral function accounting for the matrix element of the electron-phonon interaction is

$$F_\alpha(\omega) = b_\alpha \omega^2 \quad (B14)$$

with b_α a material-dependent parameter related to the electron-phonon coupling. The integral in the outgoing term can be carried out exactly to give

$$St_{out} = \frac{1}{\tau_{0,\alpha}} \left(\frac{\Delta_\alpha}{T_{c,\alpha}} \right)^3 h(\epsilon/\Delta_\alpha) f_\alpha(\epsilon) \quad (B15)$$

with $h(x) = (x^2 - 1)^{3/2}/3 + 5\sqrt{x^2 - 1}/2 - [2x + (2x)^{-1}] \ln(x + \sqrt{x^2 - 1})$. Using the notation of Ref. 65, we have introduced the material-dependent rate $\tau_{0,\alpha}^{-1} = 2\pi b_\alpha T_{c,\alpha}^3$, while the gap to critical temperature ratio to the cube is approximately 5.5 within BCS theory.

Considering first the left electrode, we multiply the kinetic equation by the density of states and integrate over all energies above Δ_L . The in and out contributions cancel out, while with our assumption of a narrow distribution function just above the gap, the recombination term gives

$$\dot{x}_L = -r^L x_L^2 \quad (B16)$$

where $r^L = (4/\tau_{0,L})(\Delta_L/T_{c,L})^3$.

For the right electrode, we consider separately the energies between Δ_R and Δ_L and above Δ_L , see Appendix B 1. After energy integration we find

$$\dot{x}_{R>} = -r^{R>} x_{R>}^2 - r^{<>} x_{R<} x_{R>} - \tau_R^{-1} x_{R>} \quad (B17)$$

$$\dot{x}_{R<} = -r^{R<} x_{R<}^2 - r^{<>} x_{R<} x_{R>} + \tau_R^{-1} x_{R>} \quad (B18)$$

where $r^{R<} = (4/\tau_{0,R})(\Delta_R/T_{c,R})^3$, $r^{<>} = r^{R<}(1 + \delta)^3/8\delta^2$, and $r^{R>} = r^{R<}(1 + \delta^2)/2\delta^2$. Note that by splitting the energy integrals, the cancellation between in and out terms is only partial, and the remaining contributions lead to the relaxation terms with $\tau_R^{-1} = r^{R<} h(\Delta_L/\Delta_R)/4$. In the calculations of the main text, we set $r^L = r^{R<}$.

4. Generation by photon-assisted tunneling

The rate of qubit transition in the presence of pair-breaking photons of frequency ω_ν is given in Ref. [34]. It takes a structure similar to that in Eq. (4), namely the sum of two terms, each the product of a matrix element times a spectral density,

$$\Gamma_{if}^{ph} = \Gamma_\nu \frac{g_T \Delta_L}{8g_K} \left[\left| \langle i | \cos \frac{\hat{\phi}}{2} | f \rangle \right|^2 S_-^{ph} \left(\frac{\omega_\nu + \omega_{if}}{\Delta_L}; \frac{\Delta_R}{\Delta_L} \right) + \left| \langle i | \sin \frac{\hat{\phi}}{2} | f \rangle \right|^2 S_+^{ph} \left(\frac{\omega_\nu + \omega_{if}}{\Delta_L}; \frac{\Delta_R}{\Delta_L} \right) \right] \quad (B19)$$

For notational simplicity, compared to Appendix A we have dropped from the state vector the parity label, since parity must change for the matrix element to be non-zero. The dimensionless prefactor Γ_ν accounts for the coupling strength between qubit and photons as well as the average number of photons [34], and we remind that ω_{if} is the energy difference between initial and final qubit states. The spectral densities

$$S_\pm^{ph}(x; z) = \int_1^\infty dy \int_z^\infty dy' \frac{yy' \pm z}{\sqrt{y^2 - 1} \sqrt{y'^2 - z^2}} \delta(x - y - y') \quad (B20)$$

generalize those of Ref. [34] to the case of unequal left/right superconducting gaps and have been defined taking the larger gap Δ_L as reference for the energy scale. Clearly, $S_\pm^{ph}(x; z) = 0$ for $x < 1 + z$.

The integral over y' in Eq. (B20) represents the integral over quasiparticle energies in the right lead; more precisely, integration over the domain $z < y' < 1$ corresponds to the contribution for energies between Δ_R and Δ_L , while that for $y' > 1$ to energies above Δ_L . Therefore, assuming $x > 2$ the ratio between $g^{R<}$ and $g^{R>}$ is given by the ratio of the expressions obtained by restricting the integral over y' to those two intervals. After integrating over y' using the δ -function and changing integration variable from y to u using $y = x - u$ for the low-energy integral and $y = 1 + xu$ in the high-energy one, we find that at leading order in $x \gg 1$ the ratio is given by $\sqrt{1 - z^2}/x$. Therefore, for large photon energy we arrive at $g^{R<}/g^{R>} \simeq \sqrt{\Delta_L^2 - \Delta_R^2}/\omega_\nu \ll 1$.

Appendix C: Split transmon

A split transmon comprises a superconducting ring interrupted by two Josephson junctions. Nonetheless, the system has a single degree of freedom $\hat{\phi}$, due to the fluxoid quantization condition $\varphi_1 + \varphi_2 = 2\pi f$; here $f = \Phi/\Phi_0$, Φ is the external flux piercing the ring, Φ_0 is the magnetic flux quantum, and φ_1 and φ_2 are the phase differences across the two junctions. The qubit Hamiltonian can be written as

$$\hat{H}_\varphi = 4E_C(\hat{N} - n_g)^2 - E_J(f) \cos(\hat{\phi} - \vartheta) \quad (C1)$$

which represents an effective single-junction qubit with flux-tunable Josephson energy

$$E_J(f) = (E_J^1 + E_J^2) |\cos \pi f| \sqrt{1 + d^2 \tan^2(\pi f)} \equiv E_J^\Sigma \mathcal{G}(f, d) \quad (\text{C2})$$

where in the last equality we defined $E_J^\Sigma = E_J^1 + E_J^2$ and $\mathcal{G}(f, d) = |\cos \pi f| \sqrt{1 + d^2 \tan^2 \pi f}$. In these expressions, $d = (E_J^1 - E_J^2)/(E_J^1 + E_J^2)$ accounts for the asymmetry between the two junctions of the transmon, and $\tan \vartheta = d \tan(\pi f)$.

1. Transition rates and matrix elements

The transition rates for a split-transmon are obtained through a generalization of the single-junction results [27],

$$\Gamma_{i \rightarrow f} = \sum_{n=1,2} \left| \langle i | \sin \frac{\hat{\varphi}_n}{2} | f \rangle \right|^2 E_J^n \tilde{S}_{\text{qp}}^{+,n}(\omega_{if}) \quad (\text{C3})$$

$$+ \left| \langle i | \cos \frac{\hat{\varphi}_n}{2} | f \rangle \right|^2 E_J^n \tilde{S}_{\text{qp}}^{-,n}(\omega_{if}),$$

where each spectral density has been scaled to the respective Josephson energy, that is, $\tilde{S}_{\text{qp}}^{\pm,n} = S_{\text{qp}}^{\pm,n}/E_J^n$. Similar to the effective Josephson energy, the matrix elements are functions of the scaled flux, and they can be calculated as in the single-junction transmon using the relations $\hat{\varphi}_n = \pi f \pm (\vartheta + \hat{\phi})$ (+ for $n = 2$ and - for $n = 1$). At leading order in $E_C/E_J(f)$ we find (with j denoting parity)

$$\left| \langle 1j | \sin \frac{\hat{\varphi}_n}{2} | 0\bar{j} \rangle \right|^2 \simeq \left[\frac{E_C}{8E_J(f)} \right]^{1/2} \frac{1 + \cos(\pi f \pm \vartheta)}{2}, \quad (\text{C4})$$

$$\left| \langle ij | \sin \frac{\hat{\varphi}_n}{2} | i\bar{j} \rangle \right|^2 \simeq \frac{1 - \cos(\pi f \pm \vartheta)}{2}, \quad (\text{C5})$$

$$\left| \langle ij | \cos \frac{\hat{\varphi}_n}{2} | i\bar{j} \rangle \right|^2 \simeq \frac{1 + \cos(\pi f \pm \vartheta)}{2}, \quad (\text{C6})$$

$$\left| \langle 1j | \cos \frac{\hat{\varphi}_n}{2} | 0\bar{j} \rangle \right|^2 \simeq \left[\frac{E_C}{8E_J(f)} \right]^{1/2} \frac{1 - \cos(\pi f \pm \vartheta)}{2}, \quad (\text{C7})$$

up to exponentially small corrections of the form given in Appendix A.

The rates entering Eqs. (11)-(13) for the split transmon are obtained after summing the contributions from the two junctions, Eq. (C3); they can be found from those of the single-junction transmon, Eqs. (B4)-(B10), upon the substitutions

$$g_T \rightarrow g_T^\Sigma, \quad \omega_{10} \rightarrow \omega_{10}(f) \quad (\text{C8})$$

$$s_{10} \rightarrow s_{10}(f) = [E_C/8E_J(f)]^{1/4} \quad (\text{C9})$$

where $g_T^\Sigma = g_T^1 + g_T^2$ is the sum of the conductances of the two junctions, and upon multiplication of the last term

in the right-most numerator by $\mathcal{G}(f, d)$. Taking Eq. (B6) as an example, this procedure gives

$$\tilde{\Gamma}_{10}^L \simeq s_{10}^2(f) \frac{g_T^\Sigma \Delta_L}{e^2} \frac{\Delta_L + \omega_{10}(f) + \mathcal{G}(f, d) \Delta_R}{\sqrt{[\Delta_L + \omega_{10}(f)]^2 - \Delta_R^2}}. \quad (\text{C10})$$

2. Generation rates for a split transmon

Analogously to the quasiparticle tunneling transition rates in Eq. (C3), the photon-assisted rates can be obtained through a generalization of Eq. (B19),

$$\Gamma_{if} = \Gamma_\nu \sum_{n=1,2} \frac{g_T^n \Delta_L}{8g_K} \left[S_-^{ph} \left(\frac{\omega_\nu + \omega_{if}}{\Delta_L}; \frac{\Delta_R}{\Delta_L} \right) \quad (\text{C11}) \right.$$

$$\left. \left| \langle i | \cos \frac{\hat{\varphi}_n}{2} | f \rangle \right|^2 + S_+^{ph} \left(\frac{\omega_\nu + \omega_{if}}{\Delta_L}; \frac{\Delta_R}{\Delta_L} \right) \left| \langle i | \sin \frac{\hat{\varphi}_n}{2} | f \rangle \right|^2 \right].$$

Using the expressions for the matrix elements of Sec. C 1, we can write the parity switching rates as

$$\Gamma_{00}^{ph} \approx \Gamma_{11}^{ph} \approx \Gamma_\nu \frac{g_T^\Sigma \Delta_L}{16g_K} [S_+^{ph} + S_-^{ph} - (S_+^{ph} - S_-^{ph}) \mathcal{G}(f, d)] \quad (\text{C12})$$

where the arguments of the spectral functions are ω_ν/Δ_L and Δ_R/Δ_L , and the relaxation/excitation rates as

$$\Gamma_{10}^{ph} \approx \Gamma_{01}^{ph} \approx \Gamma_\nu \frac{E_C}{\omega_{10}(f)} \frac{g_T^\Sigma \Delta_L}{16g_K} \quad (\text{C13})$$

$$[S_+^{ph} + S_-^{ph} + (S_+^{ph} - S_-^{ph}) \mathcal{G}(f, d)]$$

where the arguments of the spectral functions are $[\omega_\nu \pm \omega_{10}(f)]/\Delta_L$ and Δ_R/Δ_L (+ for qubit relaxation, - for excitation).

In the limit of high photon energy $\omega_\nu \gg 2\Delta_L$, we can neglect the qubit frequency $\omega_{10}(f)$ in comparison with ω_ν , approximate $S_-^{ph}(\omega_\nu/\Delta_L, \Delta_R/\Delta_L) \approx S_+^{ph}(\omega_\nu/\Delta_L, \Delta_R/\Delta_L)$, and rewrite the total generation rate per single lead as

$$\Gamma_{10}^{ph} + \Gamma_{00}^{ph} = \Gamma^{ph} \left[\frac{1}{\sqrt{\mathcal{G}(f, d)}} + \sqrt{\frac{8E_J^\Sigma}{E_C}} \right] \quad (\text{C14})$$

where

$$\Gamma^{ph} \equiv \Gamma_{10}^{ph}(\tilde{\Phi} = 0) = \Gamma_\nu \frac{E_C}{\omega_{10}(0)} \frac{g_T^\Sigma \Delta_L}{8g_K} S_+^{ph} \left(\frac{\omega_\nu}{\Delta_L}, \frac{\Delta_R}{\Delta_L} \right). \quad (\text{C15})$$

Note that since $d \leq \mathcal{G}(f, d) \leq 1$, a strong dependence on flux in Eq. (C14) is possible only for small asymmetry $d \ll E_C/8E_J^\Sigma$. However, we remind that the approximation $S_-^{ph} \approx S_+^{ph}$ is valid only in the limit of large photon frequency; for frequencies closer to $\Delta_L + \Delta_R$, we cannot neglect the terms proportional to \mathcal{G} in Eqs. (C12) and (C13), and hence a stronger dependence on flux is expected.

-
- [1] M. R. Vissers, J. Gao, D. S. Wisbey, D. A. Hite, C. C. Tsuei, A. D. Corcoles, M. Steffen, and D. P. Pappas, Low loss superconducting titanium nitride coplanar waveguide resonators, *Appl. Phys. Lett.* **97**, 232509 (2010).
- [2] R. Barends, N. Vercruyssen, A. Endo, P. J. de Visser, T. Zijlstra, T. M. Klapwijk, P. Diener, S. J. C. Yates, and J. J. A. Baselmans, Minimal resonator loss for circuit quantum electrodynamics, *Appl. Phys. Lett.* **97**, 023508 (2010).
- [3] N. Samkharadze, A. Bruno, P. Scarlino, G. Zheng, D. P. DiVincenzo, L. DiCarlo, and L. M. K. Vandersypen, High-kinetic-inductance superconducting nanowire resonators for circuit qed in a magnetic field, *Phys. Rev. Applied* **5**, 044004 (2016).
- [4] H. Rotzinger, S. T. Skacel, M. Pfirrmann, J. N. Voss, J. Münzberg, S. Probst, P. Bushev, M. P. Weides, A. V. Ustinov, and J. E. Mooij, Aluminium-oxide wires for superconducting high kinetic inductance circuits, *Supercond. Sci. Technol.* **30**, 025002 (2016).
- [5] L. Grünhaupt, N. Maleeva, S. T. Skacel, M. Calvo, F. Levy-Bertrand, A. V. Ustinov, H. Rotzinger, A. Monfardini, G. Catelani, and I. M. Pop, Loss mechanisms and quasiparticle dynamics in superconducting microwave resonators made of thin-film granular aluminum, *Phys. Rev. Lett.* **121**, 117001 (2018).
- [6] N. Maleeva, L. Grünhaupt, T. Klein, F. Levy-Bertrand, O. Dupre, M. Calvo, F. Valenti, P. Winkel, F. Friedrich, W. Wernsdorfer, A. V. Ustinov, H. Rotzinger, A. Monfardini, M. V. Fistul, and I. M. Pop, Circuit quantum electrodynamics of granular aluminum resonators, *Nat. Commun.* **9**, 3889 (2018).
- [7] J. B. Chang, M. R. Vissers, A. D. Corcoles, M. Sandberg, J. Gao, D. W. Abraham, J. M. Chow, J. M. Gambetta, M. Beth Rothwell, G. A. Keefe, M. Steffen, and D. P. Pappas, Improved superconducting qubit coherence using titanium nitride, *Appl. Phys. Lett.* **103**, 012602 (2013).
- [8] B. G. Christensen, C. D. Wilen, A. Opremcak, J. Nelson, F. Schlenker, C. H. Zimonick, L. Faoro, L. B. Ioffe, Y. J. Rosen, J. L. DuBois, B. L. T. Plourde, and R. McDermott, Anomalous charge noise in superconducting qubits, *Phys. Rev. B* **100**, 140503 (2019).
- [9] R. T. Gordon, C. E. Murray, C. Kurter, M. Sandberg, S. A. Hall, K. Balakrishnan, R. Shelby, B. Wacaser, A. A. Stabile, J. W. Sleight, M. Brink, M. B. Rothwell, K. P. Rodbell, O. Dial, and M. Steffen, Environmental radiation impact on lifetimes and quasiparticle tunneling rates of fixed-frequency transmon qubits, *Appl. Phys. Lett.* **120**, 074002 (2022).
- [10] A. P. M. Place, L. V. H. Rodgers, P. Mundada, B. M. Smitham, M. Fitzpatrick, Z. Leng, A. Premkumar, J. Bryon, A. Vrajitoarea, S. Sussman, G. Cheng, T. Madhavan, H. K. Babla, X. H. Le, Y. Gang, B. Jäck, A. Gyeenis, N. Yao, R. J. Cava, N. P. de Leon, and A. A. Houck, New material platform for superconducting transmon qubits with coherence times exceeding 0.3 milliseconds, *Nat. Commun.* **12**, 1779 (2021).
- [11] C. Wang, X. Li, H. Xu, Z. Li, J. Wang, Z. Yang, Z. Mi, X. Liang, T. Su, C. Yang, G. Wang, W. Wang, Y. Li, M. Chen, C. Li, K. Linghu, J. Han, Y. Zhang, Y. Feng, Y. Song, T. Ma, J. Zhang, R. Wang, P. Zhao, W. Liu, G. Xue, Y. Jin, and H. Yu, Towards practical quantum computers: transmon qubit with a lifetime approaching 0.5 milliseconds, *npj Quantum Inf.* **8**, 3 (2022).
- [12] D. M. Tennant, L. A. Martinez, K. M. Beck, S. R. O’Kelley, C. D. Wilen, R. McDermott, J. L. DuBois, and Y. J. Rosen, Low frequency correlated charge noise measurements across multiple energy transitions in a tantalum transmon (2021), arXiv:2106.08406 [quant-ph].
- [13] A. J. Annunziata, D. F. Santavicca, L. Frunzio, G. Catelani, M. J. Rooks, A. Frydman, and D. E. Prober, Tunable superconducting nanoinductors, *Nanotechnology* **21**, 445202 (2010).
- [14] D. Niepce, J. Burnett, and J. Bylander, High kinetic inductance NbN nanowire superinductors, *Phys. Rev. Applied* **11**, 044014 (2019).
- [15] T. M. Hazard, A. Gyeenis, A. Di Paolo, A. T. Asfaw, S. A. Lyon, A. Blais, and A. A. Houck, Nanowire superinductance fluxonium qubit, *Phys. Rev. Lett.* **122**, 010504 (2019).
- [16] M. Pita-Vidal, A. Bargerbos, C.-K. Yang, D. J. van Woerkom, W. Pfaff, N. Haider, P. Krogstrup, L. P. Kouwenhoven, G. de Lange, and A. Kou, Gate-tunable field-compatible fluxonium, *Phys. Rev. Applied* **14**, 064038 (2020).
- [17] L. Grünhaupt, M. Spiecker, D. Gusenkova, N. Maleeva, S. T. Skacel, I. Takmakov, F. Valenti, P. Winkel, H. Rotzinger, W. Wernsdorfer, A. V. Ustinov, and I. M. Pop, Granular aluminium as a superconducting material for high-impedance quantum circuits, *Nat. Mater.* **18**, 816 (2019).
- [18] M. Tinkham, *Introduction to Superconductivity*, Dover Books on Physics Series (Dover Publications, New York, 2004).
- [19] G. Catelani, X. S. Wu, and P. W. Adams, Fermi-liquid effects in the gapless state of marginally thin superconducting films, *Phys. Rev. B* **78**, 104515 (2008).
- [20] Y. Ivry, C.-S. Kim, A. E. Dane, D. De Fazio, A. N. McCaughan, K. A. Sunter, Q. Zhao, and K. K. Berggren, Universal scaling of the critical temperature for thin films near the superconducting-to-insulating transition, *Phys. Rev. B* **90**, 214515 (2014).
- [21] O. A. E. Cherney and J. Shewchun, Enhancement of superconductivity in thin aluminium films, *Can. J. Phys.* **47**, 1101 (1969).
- [22] P. Chubov, V. Eremenko, and Y. A. Pilipenko, Dependence of the critical temperature and energy gap on the thickness of superconducting aluminum films, *Sov. Phys. JETP* **28**, 389 (1969).
- [23] R. Meservey and P. M. Tedrow, Properties of very thin aluminum films, *J. Appl. Phys.* **42**, 51 (1971).
- [24] N. A. Court, A. J. Ferguson, and R. G. Clark, Energy gap measurement of nanostructured aluminium thin films for single cooper-pair devices, *Supercond. Sci. Technol.* **21**, 015013 (2007).
- [25] J. Koch, T. M. Yu, J. Gambetta, A. A. Houck, D. I. Schuster, J. Majer, A. Blais, M. H. Devoret, S. M. Girvin, and R. J. Schoelkopf, Charge-insensitive qubit design derived from the cooper pair box, *Phys. Rev. A* **76**, 042319 (2007).
- [26] G. Catelani, J. Koch, L. Frunzio, R. J. Schoelkopf, M. H. Devoret, and L. I. Glazman, Quasiparticle relaxation of

- superconducting qubits in the presence of flux, Phys. Rev. Lett. **106**, 077002 (2011).
- [27] G. Catelani, R. J. Schoelkopf, M. H. Devoret, and L. I. Glazman, Relaxation and frequency shifts induced by quasiparticles in superconducting qubits, Phys. Rev. B **84**, 064517 (2011).
- [28] A. Barone and G. Paternò, *Physics and applications of the Josephson effect* (Wiley, New York, 1982).
- [29] G. Catelani, Parity switching and decoherence by quasiparticles in single-junction transmons, Phys. Rev. B **89**, 094522 (2014).
- [30] L. I. Glazman and G. Catelani, Bogoliubov Quasiparticles in Superconducting Qubits, SciPost Phys. Lect. Notes, **31** (2021).
- [31] This expression is derived from the critical current (I_c) of an asymmetric Josephson junction [28], through the expression $E_J = \hbar I_c / (2e)$, and it is valid in the low quasiparticle density limit.
- [32] G. Catelani and D. M. Basko, Non-equilibrium quasiparticles in superconducting circuits: photons vs. phonons, SciPost Phys. **6**, 13 (2019).
- [33] K. Serniak, M. Hays, G. de Lange, S. Diamond, S. Shankar, L. D. Burkhardt, L. Frunzio, M. Houzet, and M. H. Devoret, Hot nonequilibrium quasiparticles in transmon qubits, Phys. Rev. Lett. **121**, 157701 (2018).
- [34] M. Houzet, K. Serniak, G. Catelani, M. H. Devoret, and L. I. Glazman, Photon-assisted charge-parity jumps in a superconducting qubit, Phys. Rev. Lett. **123**, 107704 (2019).
- [35] A. Rothwarf and B. N. Taylor, Measurement of recombination lifetimes in superconductors, Phys. Rev. Lett. **19**, 27 (1967).
- [36] X. Y. Jin, A. Kamal, A. P. Sears, T. Gudmundsen, D. Hover, J. Miloshi, R. Slattery, F. Yan, J. Yoder, T. P. Orlando, S. Gustavsson, and W. D. Oliver, Thermal and residual excited-state population in a 3d transmon qubit, Phys. Rev. Lett. **114**, 240501 (2015).
- [37] U. Vool, I. M. Pop, K. Sliwa, B. Abdo, C. Wang, T. Brecht, Y. Y. Gao, S. Shankar, M. Hatridge, G. Catelani, M. Mirrahimi, L. Frunzio, R. J. Schoelkopf, L. I. Glazman, and M. H. Devoret, Non-poissonian quantum jumps of a fluxonion qubit due to quasiparticle excitations, Phys. Rev. Lett. **113**, 247001 (2014).
- [38] H. Paik, D. I. Schuster, L. S. Bishop, G. Kirchmair, G. Catelani, A. P. Sears, B. R. Johnson, M. J. Reagor, L. Frunzio, L. I. Glazman, S. M. Girvin, M. H. Devoret, and R. J. Schoelkopf, Observation of high coherence in Josephson junction qubits measured in a three-dimensional circuit qed architecture, Phys. Rev. Lett. **107**, 240501 (2011).
- [39] X. Pan, H. Yuan, Y. Zhou, L. Zhang, J. Li, S. Liu, Z. H. Jiang, G. Catelani, L. Hu, and F. Yan, Engineering superconducting qubits to reduce quasiparticles and charge noise (2022).
- [40] A. P. Vepsäläinen, A. H. Karamlou, J. L. Orrell, A. S. Dogra, B. Loer, F. Vasconcelos, D. K. Kim, A. J. Melville, B. M. Niedzielski, J. L. Yoder, S. Gustavsson, J. A. Formaggio, B. A. VanDevender, and W. D. Oliver, Impact of ionizing radiation on superconducting qubit coherence, Nature **584**, 551 (2020).
- [41] L. Cardani, F. Valenti, N. Casali, G. Catelani, T. Charpentier, M. Clemenza, I. Colantoni, A. Cruciani, G. D'Imperio, L. Gironi, L. Grünhaupt, D. Gusenkova, F. Henriques, M. Lagoin, M. Martinez, G. Pettinari, C. Rusconi, O. Sander, C. Tomei, A. V. Ustinov, M. Weber, W. Wernsdorfer, M. Vignati, S. Pirro, and I. M. Pop, Reducing the impact of radioactivity on quantum circuits in a deep-underground facility, Nat. Commun. **12**, 10.1038/s41467-021-23032-z (2021).
- [42] M. McEwen, L. Faoro, K. Arya, A. Dunsworth, T. Huang, S. Kim, B. Burkett, A. Fowler, F. Arute, J. C. Bardin, A. Bengtsson, A. Bilmes, B. B. Buckley, N. Bushnell, Z. Chen, R. Collins, S. Demura, A. R. Derk, C. Erickson, M. Giustina, S. D. Harrington, S. Hong, E. Jeffrey, J. Kelly, P. V. Klimov, F. Kostritsa, P. Laptev, A. Locharla, X. Mi, K. C. Miao, S. Montazeri, J. Mutus, O. Naaman, M. Neeley, C. Neill, A. Opremcak, C. Quintana, N. Redd, P. Roushan, D. Sank, K. J. Satzinger, V. Shvarts, T. White, Z. J. Yao, P. Yeh, J. Yoo, Y. Chen, V. Smelyanskiy, J. M. Martinis, H. Neven, A. Megrant, L. Ioffe, and R. Barends, Resolving catastrophic error bursts from cosmic rays in large arrays of superconducting qubits, Nat. Phys. **18**, 107 (2021).
- [43] C. D. Wilen, S. Abdullah, N. A. Kurinsky, C. Stanford, L. Cardani, G. D'Imperio, C. Tomei, L. Faoro, L. B. Ioffe, C. H. Liu, A. Opremcak, B. G. Christensen, J. L. DuBois, and R. McDermott, Correlated charge noise and relaxation errors in superconducting qubits, Nature **594**, 369 (2021).
- [44] F. Henriques, F. Valenti, T. Charpentier, M. Lagoin, C. Gouriou, M. Martínez, L. Cardani, M. Vignati, L. Grünhaupt, D. Gusenkova, J. Ferrero, S. T. Skacel, W. Wernsdorfer, A. V. Ustinov, G. Catelani, O. Sander, and I. M. Pop, Phonon traps reduce the quasiparticle density in superconducting circuits, Appl. Phys. Lett. **115**, 212601 (2019).
- [45] V. Iaia, J. Ku, A. Ballard, C. P. Larson, E. Yelton, C. H. Liu, S. Patel, R. McDermott, and B. L. T. Plourde, Phonon downconversion to suppress correlated errors in superconducting qubits (2022).
- [46] P. A. Spring, S. Cao, T. Tsunoda, G. Campanaro, S. D. Fasciati, J. Wills, V. Chidambaram, B. Shteynas, M. Bakr, P. Gow, L. Carpenter, J. Gates, B. Vlastakis, and P. J. Leek, High coherence in a tileable 3d integrated superconducting circuit architecture (2021), arXiv:2107.11140 [quant-ph].
- [47] C. Kurter, C. E. Murray, R. T. Gordon, B. B. Wymore, M. Sandberg, R. M. Shelby, A. Eddins, V. P. Adiga, A. D. K. Finck, E. Rivera, A. A. Stabile, B. Trimm, B. Wacaser, K. Balakrishnan, A. Pyzyrna, J. Sleight, M. Steffen, and K. Rodbell, Quasiparticle tunneling as a probe of Josephson junction barrier and capacitor material in superconducting qubits (2022), arXiv:2106.11488 [quant-ph].
- [48] C. Wang, Y. Y. Gao, I. M. Pop, U. Vool, C. Axline, T. Brecht, R. W. Heeres, L. Frunzio, M. H. Devoret, G. Catelani, L. I. Glazman, and R. J. Schoelkopf, Nat. Commun. **5**, 5836 (2014).
- [49] Note that the approximation $g^{R<} \approx 0$ is particularly accurate in this case, due to the limited width of the quasiparticle energy window between Δ_R and Δ_L .
- [50] In our modeling $\Gamma_{\text{ex}} = 2\Gamma^{ph} + \Gamma_{10}^{ee}$ is the inverse lifetime of the qubit in the absence of nonequilibrium quasiparticles.
- [51] The solutions are obtained through a find-root procedure, setting to zero time derivative terms.
- [52] This value is computed using Eq. 3 in Ref. [48], using the parameters in the supplementary material for device B2 ω_{10} , $T_1 = T_1(B \sim 0 \text{ mG})$, and $\Gamma_{\text{ex}} = T_1^{-1}(B \sim 100 \text{ mG})$.

- [53] For the consistency of the set of equations, the term $r^{R<>}$ must be dropped also in the last equation. This approximation works well for $x_{R>} \ll x_{R<}$.
- [54] K. Serniak, S. Diamond, M. Hays, V. Fatemi, S. Shankar, L. Frunzio, R. Schoelkopf, and M. Devoret, Direct dispersive monitoring of charge parity in offset-charge-sensitive transmons, *Phys. Rev. Applied* **12**, 014052 (2019).
- [55] C.-H. Liu, D. C. Harrison, S. Patel, C. D. Wilen, O. Raftery, A. Shearow, A. Ballard, V. Iaiia, J. Ku, B. L. T. Plourde, and R. McDermott, Quasiparticle poisoning of superconducting qubits from resonant absorption of pair-breaking photons (2022).
- [56] M. Spiecker, P. Paluch, N. Drucker, S. Matityahu, D. Gusenkova, N. Gosling, S. Günzler, D. Rieger, I. Taktmakov, F. Valenti, P. Winkel, R. Gebauer, O. Sander, G. Catelani, A. Shnirman, A. V. Ustinov, W. Wernsdorfer, Y. Cohen, and I. M. Pop, A quantum szilard engine for two-level systems coupled to a qubit (2022).
- [57] G. Catelani and D. M. Basko, Non-equilibrium quasiparticles in superconducting circuits: photons vs. phonons, *SciPost Phys.* **6**, 13 (2019).
- [58] R.-P. Riwar, A. Hosseinkhani, L. D. Burkhardt, Y. Y. Gao, R. J. Schoelkopf, L. I. Glazman, and G. Catelani, Normal-metal quasiparticle traps for superconducting qubits, *Phys. Rev. B* **94**, 104516 (2016).
- [59] As temperature increases, quasiparticle can escape the trap due to thermal activation by phonons, see [39].
- [60] R.-P. Riwar and G. Catelani, Efficient quasiparticle traps with low dissipation through gap engineering, *Phys. Rev. B* **100**, 144514 (2019).
- [61] J. Krause, C. Dickel, E. Vaal, M. Vielmetter, J. Feng, R. Bounds, G. Catelani, J. M. Fink, and Y. Ando, Magnetic field resilience of three-dimensional transmons with thin-film $\text{al}/\text{al}_x/\text{Al}$ josephson junctions approaching 1 t, *Phys. Rev. Applied* **17**, 034032 (2022).
- [62] A peak in the total parity switching rate $\Gamma_{10}^{e\sigma} + \Gamma_{11}^{e\sigma}$ has been experimentally reported in Ref. 64 during the completion of this manuscript.
- [63] V. E. Manucharyan, J. Koch, L. I. Glazman, and M. H. Devoret, Fluxonium: Single cooper-pair circuit free of charge offsets, *Science* **326**, 113 (2009).
- [64] S. Diamond, V. Fatemi, M. Hays, H. Nho, P. D. Kurilovich, T. Connolly, V. R. Joshi, K. Serniak, L. Frunzio, L. I. Glazman, and M. H. Devoret, Distinguishing parity-switching mechanisms in a superconducting qubit (2022).
- [65] S. B. Kaplan, C. C. Chi, D. N. Langenberg, J. J. Chang, S. Jafarey, and D. J. Scalapino, Quasiparticle and phonon lifetimes in superconductors, *Phys. Rev. B* **14**, 4854 (1976).
- [66] J.-J. Chang and D. J. Scalapino, Kinetic-equation approach to nonequilibrium superconductivity, *Phys. Rev. B* **15**, 2651 (1977).